Influence of dielectric layers on the optomechanical properties of polymer membranes in a fiber cavity

Andreas Reuß

Masterarbeit in Physik
angefertigt im Physikalischen Institut

vorgelegt der
Mathematisch-Naturwissenschaftlichen Fakultät
der
Rheinischen Friedrich-Wilhelms-Universität
Bonn

Mai 2023

I hereby declare that this thesis was formulated by myself and that no sources or tools other than those cited were used.

Bonn, 15.05.23 ....

Date Signature

1. Gutachter: Prof. Stefan Linden
2. Gutachter: Prof. Sebastian Hofferberth

Contents

CHAPTER 1

Introduction

Cavity optomechanics is a field of research studying the interaction of electromagnetic radiation with mechanical motion, which allows for new approaches to study the effects of radiation pressures on small mechanical systems down to quantum mechanical scales. While having its origins in the study of gravitational wavedetectors in the 1970s[1] and the pioneering works by V. Braginsky *et al.* in optomechancial microwave systems in the late 1960s [2], this field nowadays offers a large variety of tools to investigate the interaction of electromagnetic radiation with mechanical systems, ranging from macroscopic ($m \sim$ kg) to microscopic scales ($m \sim 10^{-20}$g) [3].

The developments in recent years in this field, like the fabrication of better micro systems, and the high sensitivity of these optomechancial systems to mass and frequency changes allow for a variety of applications ranging from ultra sensitive force measurements to applications in quantum computing like quantum memories or quantum repeaters[4]. Optomechancial interaction further offers a new tool to investigate interesting nonlinear quantum effects like strong coupling or sideband resolved cooling by dynamical back action[5, 6].

While the simplest optomechanical systems feature a Fabry Pérot cavity with a suspended end mirror in an optical cavity [5] or LC circuits with moving capacitor in the microwave regime [2], many other experimental approaches have been realized like cold atomic clouds [7] or oscillating photonic crystal waveguides [8], just to name a few.

It is however difficult to realize high finesse $\mathcal{F}$ cavities with a high Q mechanical oscillator in a single device. An alternative approach is to place a thin dielectric membrane between two mirrors to form a membrane-in-the-middle (MIM) system, in which the cavity detuning depends on the membrane position. Such applications, mostly using materials like silicon nitride (SiN), could achieve qualities of $Q = 10^6 - 10^7$ at room to cryogenic temperatures[9, 10].

A rather new approach in realising compact membrane-in-the-middle systems is by using direct laser writing to place a polymer drum directly on one end mirror inside a hybrid fiber cavity. This design offers a great platform in building high finesse cavities within the micrometer regime. Commercial direct laser writing systems, like the *NanoScribe Photonics Professional GT+*, allow for an easy and precise fabrication of multiple of these high finesse MIM systems. Such systems have been successfully implemented by our group and despite their low reflectivity these MIM systems show rather high optomechanical couplingstrengths (> 25 kHz) [11].

However, a disadvantage of these polymer drum systems are their comparably high mechanical losses due to the viscous nature of the polymer material [12, 13]. For realizing high mechanical qualities ($Q \sim 600$) these systems so far rely on cryogenic temperatures to reduce internal damping losses [11].

To improve the performance of the polymer membranes at room temperature, a dielectric material with better mechanical properties could be deposited on top of the polymer membranes. With increased overall young's modulus the membrane would become stiffer, which enhances its oscillatory behaviour and therefore the overall mechanical quality could be improved.

Since these direct laser written MIM systems are still a subject of research in our group, the aim of this thesis was to investigate to what extend dielectric layer deposition on top of the drums, with materials like magnesium fluoride MgF_2, could improve their mechanical properties. The polymer membranes were supposed to be eventually replaced by the low loss dielectric layers. Therefore another aim of this thesis was to propose a method to completely remove said polymer membranes within the limits of direct laser writing for the drum fabrication.

This thesis presents the fabrication of the optomechanical membrane-in-the-middle-systems for a fiber cavity setup by direct laser writing and how deposited dielectric layers influence the optomechanical responses of the drums. Limitations of the fabrication process on the quality of the drums and reproducibility are discussed and optimized fabrication parameters are derived. Further a method of partial removal of the soft polymer membrane of the layered drums beneath the dielectric layers will be presented. Therefore chapter 2 and 3 will give a brief introduction into the physics of fiber cavities and optomechanical interaction as well as briefly introducing the used systems. In chapter 4 the basic mechanical properties of the used polymer membranes will be discussed and simulated. In chapter 5 the methods and steps to fabricate these layered drums will be discussed, while the results of the analysis of this thesis will be presented in chapter 6.

CHAPTER 2

Fiber Cavities

Fiber cavities offer a variety of advantages compared to conventional cavity types. The small dimensions of the fiber offer the assembly of high finesse and stable cavities with small cavity lengths. They further allow for easy access to the cavity by direct optical coupling through the fiber. With its open resonator volume these cavity types are well suited for optomechanical experiments, allowing for direct insertion of dispended membranes [11] as well as direct laser written membrane systems on the fiber cavity end mirrors, as used in this thesis.

Since the experiments were conducted in fiber Fabry Pérot cavities, this chapter is dedicated to give a short overview of the basic properties and physical principles of Fabry Pérot cavities and the fiber cavity setup used in the experiments. [14][15]

2.1 Fabry Pérot Etalon

A Fabry Pérot etalon (cavity) in its simplest form consists of two opposite mirrors (with respective reflective and transmittive coefficients r_i and t_i), which are separated by a distance L (see fig. 2.1).

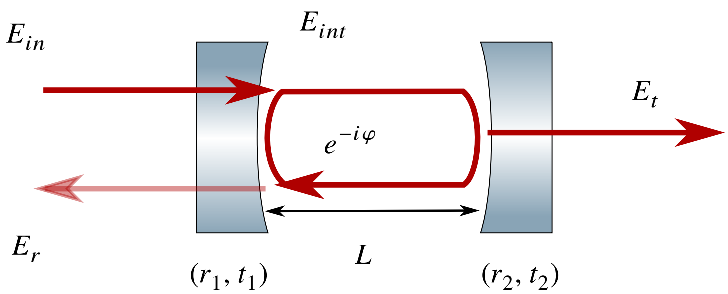

Figure 2.1: Fabry Pérot cavity with two concave mirrors (with reflectivity and transmittivity r_i, t_i), distances by cavity length L. An electromagnetic field E_{in} is coupled into the resonator, while the part E_r is reflected at the first mirror. Inside the cavity an internal field E_{int} with phase ϕ builds up and couples out a transmitted part E_t at the second mirror. In resonance the reflected part gets destructively interfered (adapted from [16])

Light, getting coupled through one of the cavity mirrors, splits up in a backreflected part and a transmitted part. The transmitted part gets reflected back and fourth between the mirrors multiple times, amplifying the lightfield inside. Further, incoupled light, which is in resonance with a cavity mode, leads to destructive interference with the reflected part at the incoupling mirror, resulting in a vanishing backreflected part. This causes a maximum lightfield inside the cavity and therefore a maximal transmittance of the entire cavity, which is given by [15]

$$\mathcal{T} = |t|^2 = \frac{|t_1 t_2 \exp(-i\varphi)|^2}{|1 - r_1 r_2 \exp(-i\varphi)|^2}$$

with phase $\varphi = 2nk_0L$.

Light, which is in resonance with the cavity, forms standing waves between the two mirrors with the resonance condition for each allowed standing wave:

$$\lambda_m = \frac{2nL}{m} \quad ; \quad \nu_m = \frac{mc_0}{2nL} \tag{2.1}$$

with $m \in \mathbb{N}\backslash\{0\}$ being the m-th longitudinal mode of the cavity and n the refractive index of the medium inside (typ. air with $n \approx 1$).

The distance between two allowed cavity modes (resonances) in frequency space is called the free spectral range and is in general given by

$$\Delta\nu_{FSR} = \nu_{m+1} - \nu_m = \frac{c_0}{2nL}$$

The cavity resonances can be displayed in frequency space as peaks (dips) in the transmission (reflection) signal with a spacing of $\Delta\nu_{FSR}$ between the resonances (see fig. 2.2).

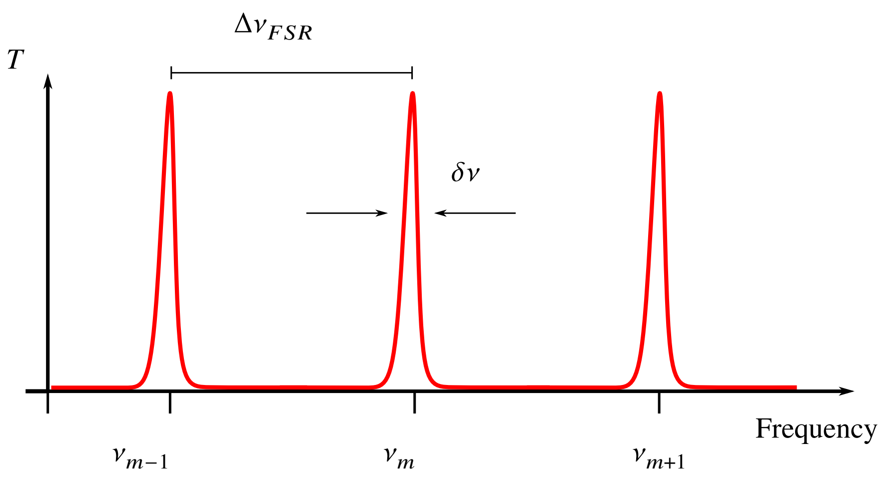

Figure 2.2: Transmission peaks of an optical cavity.

For a lossless cavity the peaks would be sharp delta functions. However, the real cavity field is not lossless, which result in a finite lifetime of the photons inside the cavity. The resonance peaks therefore are broadened and show a Lorentzian like shape with a peak width of $\delta\nu$, which is the so called spectral width and a measure for the decay rate κ of the cavity photons [15].

$$\delta\nu = \frac{\kappa}{2\pi}$$

The quality of an optical resonator is in general characterized by the dimensionless quantity $\mathcal{F}$, which is the so called finesse of a cavity. For a low loss cavity ($\mathcal{F} >> 1$) with the reflection coefficients r_1 and r_2 of both mirrors, the finesse is given by [15]:

$$\mathcal{F} = \frac{\pi\sqrt{|r_1 r_2|}}{1 - |r_1 r_2|} \approx \frac{\Delta\nu_{FSR}}{\delta\nu}$$

Cavity Losses One major source of losses inside a cavity, limiting the photon lifetime, is due to outcoupling of photons from the cavity. The nonzero transmittance of the mirrors is a main reason for outcoupling from the cavity. The finite size of the mirrors can also lead to an unstable cavity configuration, leading to leakage and diffraction losses at the mirror edges. Another reason for losses are absorption and scattering losses at the mirror surfaces and other optical components inside the beam path. The finesse can then be characterized by the loss factors of the individual losses [15]

$$\mathcal{L}_{tot} = \sum_i \mathcal{L}_i \approx \frac{2\pi\delta\nu}{c_0}$$

and the relation

$$\mathcal{F} = \frac{2\pi}{\mathcal{L}_{tot}}$$

2.1.1 Gaussian Beam

The field of the ground mode of the laser inside the cavity is best described by a Gaussian beam, which is a cylindersymmetric solution of the paraxial wave equation [15].

$$E(\rho, z, t) = E_0 \frac{W_0}{W(z)} \exp\left[-\frac{\rho^2}{W^2(z)}\right] \exp\left[-i(k_z z + k_z \frac{\rho^2}{2R(z)} - \zeta(z))\right] \exp\left[i\omega t\right] \tag{2.2}$$

It is often convenient to describe a coherent monochromatic lightsource by a monochromatic plane wave, which is a solution of the homogeneous wave equations. Since a real laserbeam doesn't form an infinite extended wave front, its field inside the cavity is better described by a Gaussian beam [16]. The beam describes a cylindersymmetric beam propagating in z-direction with diverging beam waist (2W(z)) and exponential decreasing beam (intensity) profile in xy-direction (with $x^2 + y^2 = \rho^2$). With increasing distance from the center the wave fronts become curved, while near the center they are almost plane (see fig. 2.3).

For transversal modes the beam is described with so called Laguèrre-Gauss or Hermite-Gauss beams, which introduce different phaseprofiles (see fig. 2.4) for higher order modes (For a more detailed description see [15, 16]). However, for the description of the cavity field the Gaussian ground mode description is sufficient enough. The basic Gaussian beam parameters are listed for example in table 2.1

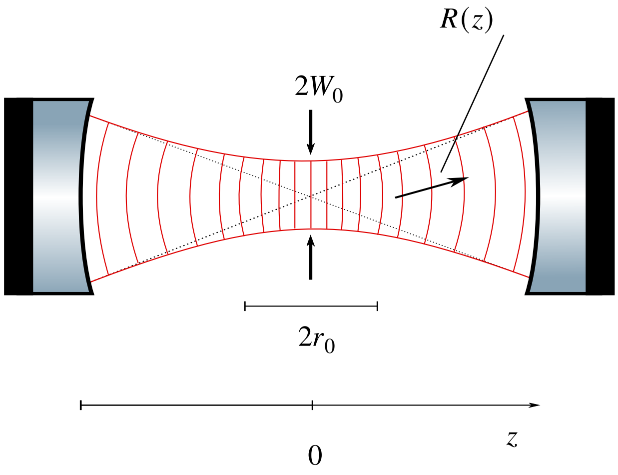

Figure 2.3: Schematic depiction of a Gaussian beam wavefronts inside a Fabry Pérot cavity with beam parameters.

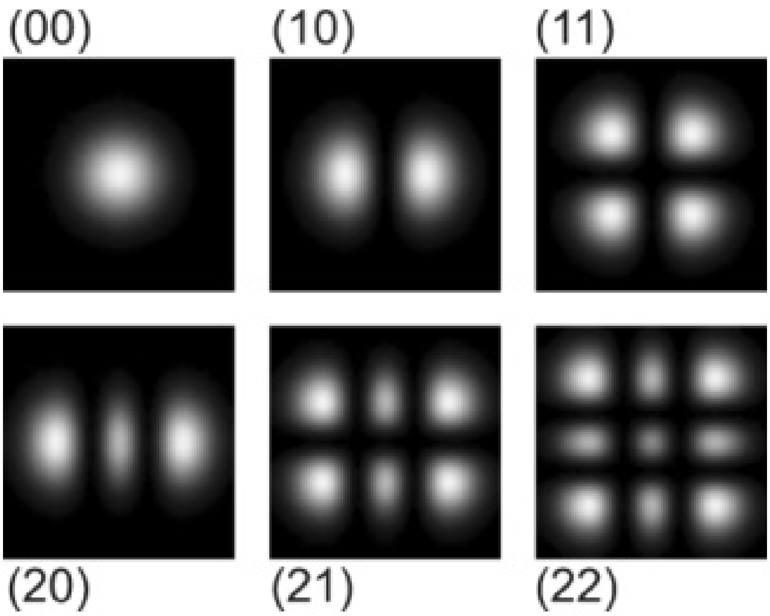

Figure 2.4: Depiction of phaseprofiles of transversal (higher order) Hermite-Gauss modes inside a cavity with the 00 mode corresponding to the Gaussian beam (taken from [16])

2.2 Fiber Cavity Setup

The fiber cavity setup, which I used for my experiments for this thesis, is in most parts the setup by Lukas Tenbrake [13]. This section gives a brief explanation of the fiber cavity and the setup it was build in.

$W_0 = \sqrt{\frac{\lambda z_0}{\pi}}$	Beamwaist radius at $z = 0$ at which beam intensity falls to $1/e$
$W(z) = W_0\sqrt{1 + (\frac{z}{z_0})^2}$	z-position dependant beam waist radius
z_0	Rayleigh length at which $W(z_0) = \sqrt{2}W_0$
$R(z) = z\sqrt{1 + (\frac{z_0}{z})^2}$	Radius of curvature of wavefronts
$\zeta(z) = \arctan(\frac{z}{z_0})$	Gouy phase shift due to radius of curvature

Table 2.1: Important beam parameters of a Gaussian beam [15].

2.2.1 Fiber Mirror

The used fiber mirrors consist of a partially reflecting optical fiber tip with a concave shaped end facet. They allow for building small and stable cavities with high finesse. A further advantage is the direct optical coupling to the cavity through the fiber. Its fabrication and usage in the experimental setup are briefly addressed in this section.

Fabrication of the Fiber Mirror The fiber mirrors used for the experiments consist of a silicon single mode stepindex fiber with a concave end facet, layered by a partial reflective coating. They are produced in two fabrication steps. In a first ablation step a high power CO_2 laser, is used to burn a hole inside the fiber end facet for a concave shape (see fig. 2.5) [17, 18]. In a second step, the fiber end facet gets coated by an external company[1] with several alternating layers of Ta_2O_5 and SiO_2 to form a distributed bragg mirror ($\lambda_0 \sim 780\,\mathrm{nm}$) on the end facet[11, 13].

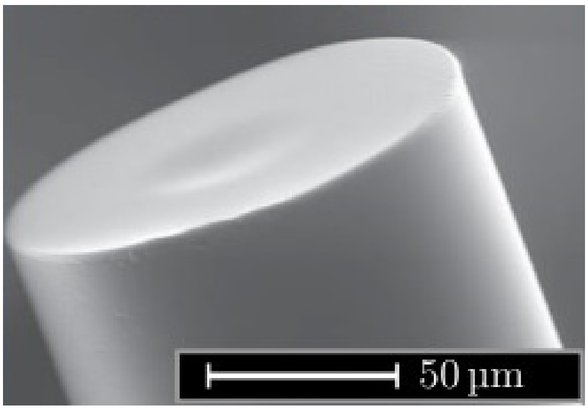

Figure 2.5: SEM image of a fiber end face after the ablation process (taken from [13, 18]).

[1] Laseroptic GmbH: `https://www.laseroptic.com`

2.2.2 Hybrid Fiber Cavity Setup

For the experiments a hybrid fiber cavity was used. It consists of a fiber mirror and a planar 0.5” (inch) distributed Bragg mirror (DBM) with 10 ppm (parts per million) transmission, on which the drums will later be printed. The DBM is mounted on a mirror holder, connected to a motorized 2D stage (see fig. 2.6). With this the mirror can be moved relative to the fiber position, to select different areas on the mirror for a cavity build. The fiber itself is placed inside a ferrule for a stable hold and glued onto a shear piezo to scan the cavity and to correct length drifts (see fig. 2.7). This setup allows for finesses of up to $\mathcal{F} \simeq 1500$ [13].

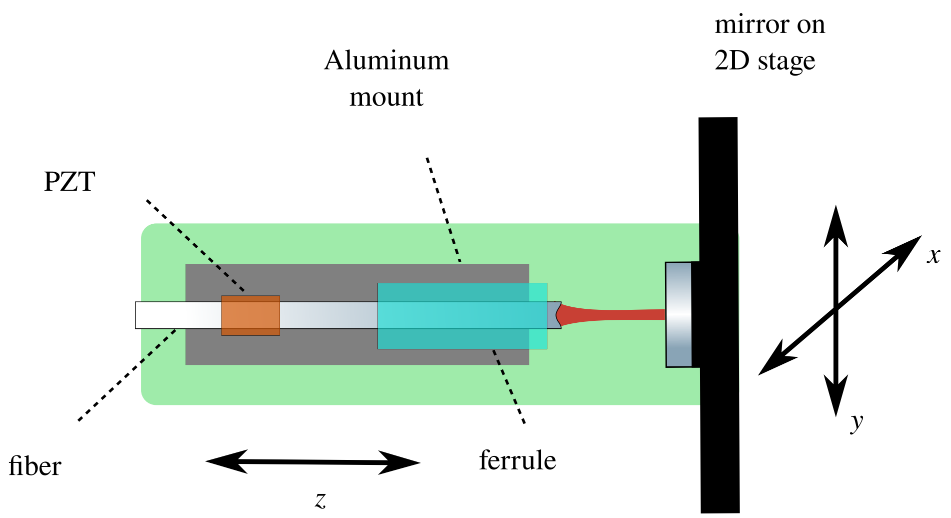

Figure 2.6: Hybrid fiber cavity setup with fiber mirror connected to piezoelectric transducer (PZT) and 0.5” Bragg mirror on 2D stage (varied from [13])

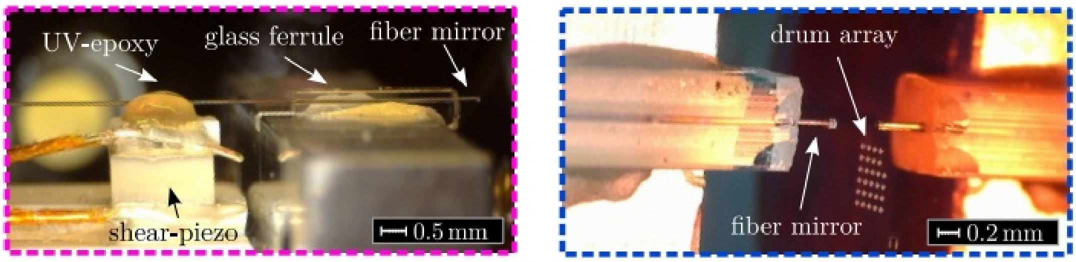

Figure 2.7: Depiction of the hybrid fiber cavity setup. (Left) Fiber mirror mounted in a glass ferrule and glued to a shear piezo for small movements of the fiber mirror. (Right) Closeup of the hybrid fiber cavity with a drum array printed on the flat 0.5” mirror (taken from [13]).

CHAPTER 3

Optomechanical Systems

The field of cavity optomechanics investigates the interaction of electromagnetic radiation with a mechanical oscillation inside an optical cavity. Such optomechanical systems in the most common form consist of a Fabry Pérot cavity with one fixed and one movable mirror, driven by radiation pressure. The systems used for this thesis, the so called membrane-in-the-middle systems, are a rather unconventional type, consisting of a suspended dielectric membrane between two cavity mirrors.

This Chapter is dedicated to explain the general physics of optomechanial interaction and the physics of optomechanical MIM systems, which are used in this thesis.

3.1 Optomechanical Interaction

The principles of optomechnical interaction inside a cavity can be best described by the so called "mirror on a spring" model. It describes a cavity, which consists of two end mirrors with one being fixed and the other being hooked to rigid wall by a mechanical spring (see fig. 3.1). Light, that gets resonantly coupled to the cavity (with ω_{cav}), builds up radiation pressure, which acts on the mirror on the spring and leads to a shift of position. This shift then leads to a change of in the cavity length (L_{cav}) and therefore to a shift of the cavity resonance frequency (see eq. (2.1)). The then detuned lightfield therefore has reduced radiation pressure, allowing the mirror to shift back, leading to an oscillation of the mirror and the intensity of the light field inside. This interaction, varying radiation pressure and mechanical motion, is then resulting in an effective coupling of the lightfield to the mechanical oscillation.

3.2 Hamiltonian Formulation

The mathematics and principles behind optomechanical coupling can be best explained with the quantum mechanical description, by interpreting the cavity field and the mechanical resonator as harmonic oscillators with optical mode ω_{cav} and mechanical mode Ω_m. This allows for a Hamiltonian formulation of the system [5]. The uncoupled system is described by the unperturbed Hamiltonian of both oscillators $\hat{H}_0$ [5]:

$$\hat{H}_0 = \hbar\omega_{cav}(\hat{a}^\dagger\hat{a} + \frac{1}{2}) + \hbar\Omega_m(\hat{b}^\dagger\hat{b} + \frac{1}{2}) \tag{3.1}$$

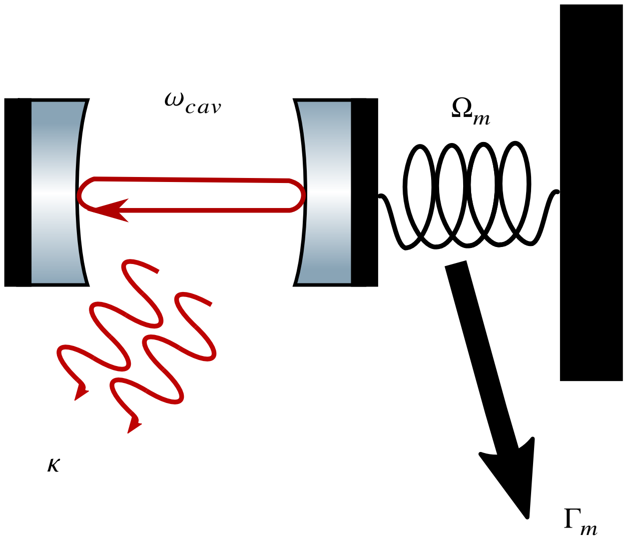

Figure 3.1: Optomechanical mirror on a spring model. The cavity lightfield ω_{cav} creates radiation pressure on the mirror connected to a spring with eigenfrequency Ω_m. The optical loss rate κ characterizes losses due to scattering, absorption and leakage radiation. Dissipative losses in the mechanical spring (with rate Γ_m) couple to a surrounding thermal bath [5].

with the creation and annihilation operators ($\hat{a}^\dagger$, $\hat{a}$) for the cavity photons and respectively for the mechanical phonons ($\hat{b}^\dagger$, $\hat{b}$), which obey the (boson) commutator relations $[\hat{a}, \hat{a}^\dagger] = [\hat{b}, \hat{b}^\dagger] = 1$. By considering small variations (δx) to the cavity length L_{cav} (due to the mechanical motion) one can expand the perturbed cavity resonance to first order [5].

$$\omega_{cav}(x) \approx \omega_{cav} + x \cdot \frac{\partial \omega_{cav}}{\partial x} + \cdots \tag{3.2}$$

With this one can rewrite the cavity Hamiltonian with the shifted frequency [5]

$$\hbar\omega_{cav}(\hat{a}^\dagger\hat{a}) \approx \hbar(\omega_{cav} - G\hat{x})\hat{a}^\dagger\hat{a} \tag{3.3}$$

where $G = \frac{\partial \omega_{cav}}{\partial x}$ is defined as the so called first order *Pullparameter*. The minus sign reflects, that positive shift in x results in a negative shift of the cavity frequency if $G > 0$. The position operator of the mechanical oscillator is given by [5]

$$\hat{x} = x_{ZPF}(\hat{b} + \hat{b}^\dagger) \tag{3.4}$$

with x_{ZPF} being the so called zero point fluctuation of the mechanical ground mode, which is given by [5]:

$$x_{ZPF} = \sqrt{\frac{\hbar}{2m_{\text{eff}}\Omega_m}} \tag{3.5}$$

The interaction Hamiltonian is then given by

$$\hat{H}_{Int} = -\hbar g_0 \hat{a}^\dagger \hat{a}(\hat{b} + \hat{b}^\dagger) \tag{3.6}$$

where

$$g_0 = x_{ZPF} G \tag{3.7}$$

is called the (linear) *vacuum optomechanical coupling strength*. It is given in dimensions of frequency and describes the fundamental interaction between a single cavity photon and a mechanical phonon. It is a measure for the coupling to the mechanical oscillator and depends on the cavity frequency shift. Compared to the optical lossrate κ in the cavity, g_0 is usually much smaller [5], which then requires a large average photon number inside the cavity $\bar{n}_{cav} = \langle \hat{a}^\dagger \hat{a} \rangle$ to enhance the coupling.

Since the radiation will always act with a constant (average) force and a fluctuating part on the mechanical oscillator [5], the cavity field operator (annihilation operator) gets split up into an average coherent amplitude $\langle \hat{a} \rangle = \bar{\alpha}$ and a fluctuating term $\delta\hat{a}$. This approach is called "linearized" approximate description of optomechanics. The field operator then reads

$$\hat{a} = \bar{\alpha} + \delta\hat{a} \tag{3.8}$$

with which the interaction Hamiltonian (see eq. (3.6)) can be rewritten as

$$\hat{H}_{Int} = -\hbar g_0 (\bar{\alpha} + \delta\hat{a})^\dagger (\bar{\alpha} + \delta\hat{a})(\hat{b} + \hat{b}^\dagger) \tag{3.9}$$

By considering only quadratic terms of $\bar{\alpha}$ and assuming without loss of generality $\bar{\alpha}^* = \bar{\alpha} = \sqrt{\bar{n}_{cav}}$, the "linearized" interaction Hamiltonian (linear in the fluctuation terms) is derived as

$$\hat{H}^{(lin)}_{Int} = -\hbar g_0 \bar{n}_{cav}(\hat{b} + \hat{b}^\dagger) - \hbar g_0 \sqrt{\bar{n}_{cav}}(\delta\hat{a}^\dagger + \delta\hat{a})(\hat{b} + \hat{b}^\dagger) \tag{3.10}$$

From the first term of this Hamiltonian one can derive a constant radiation force acting on the mechanical oscillator with $F_{\text{ext}} = -\frac{d\hat{H}}{d\hat{x}} = \hbar\bar{n}_{cav}\frac{g_0}{x_{ZPF}}$. The second term describes the fluctuating interaction of the optical and mechanical oscillator, with

$$g := g_0 \sqrt{\bar{n}_{cav}} \tag{3.11}$$

being often referred to as "optomechanical couplingstrength" [5], which becomes the vacuum coupling strength for a single cavity photon ($\bar{n}_{cav} = 1$). Since the coupling strength scales with the photon number $\bar{n}_{cav}$, a high intensity of the laser is important. For interesting regimes, like side band resolved cooling, the couplingstrength must be much higher than the mechanical and cavity losses ($g >> \kappa >> \Gamma_m$) [5].

3.3 Membrane-in-the-Middle System

The direct laser written polymer drums, used in this thesis, form a so called membrane-in-the-middle (MIM) system. This system is described by a thin membrane between the end mirrors inside a Fabry Pérot cavity (see fig. 3.2).

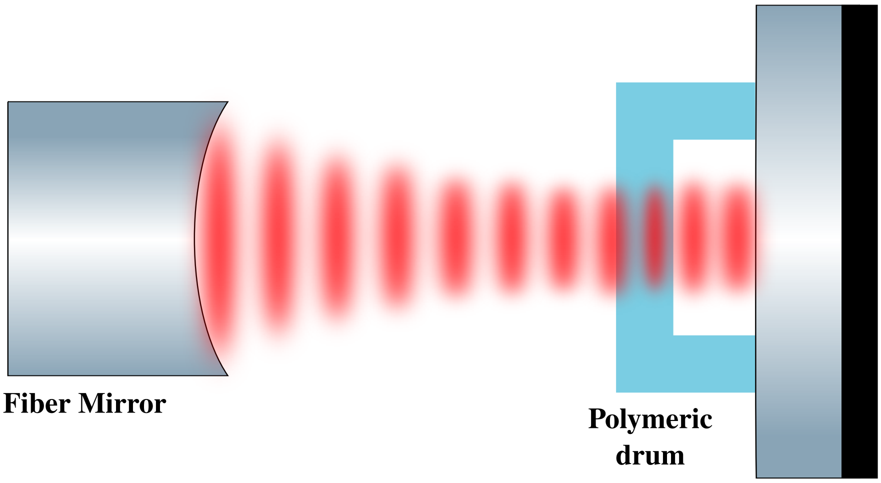

Figure 3.2: MIM-system in a hybrid fiber cavity with a direct laser written polymer drum on the planar mirror. The intensity distribution (red) of a the lightfield (Gaussian beam) is displayed throughout the cavity.

The membrane is moved by radiation pressure, due to reflection at the membrane interface. In contrast to the mirror on a spring mode, the resonance shift of the cavity is not realized by a change of the cavity length, but rather due to an effective change of the optical path length ($n_{\text{eff}}\lambda$) by varying the boundary conditions, due to the oscillating membrane position. Inside the cavity a standing wave builts up, leading to intensity maxima and minima, which result in local high and low radiation pressure areas. The high intensity areas therefore lead to regions with higher optomechanical coupling due to a higher momentum transfer and therefore a high shift of the resonance frequency (c.f. $\bar{n}_{cav}$ in eq. (3.11)). As mentioned above, the intensity distribution and therefor the optomechancial coupling inside the cavity is determined by the boundary conditions at the interfaces (surfaces), with which the fields inside the cavity can be determined.

3.3.1 Fields inside the MIM System

The optomechanical couplingstrength inside the cavity is highly dependant on the field distributions, which depend on the boundary conditions. By constructing the fields inside the cavity the theoretical resonance shifts and therefore the couplingstrength of this system can be modeled.

To understand the formation of the fields inside such a MIM system and how the theoretical couplingstrength can then be derived from it, this section will explain the analytical approach, based on classical electrodynamics[1].

[1] For a more detailed description of this approach see [13]

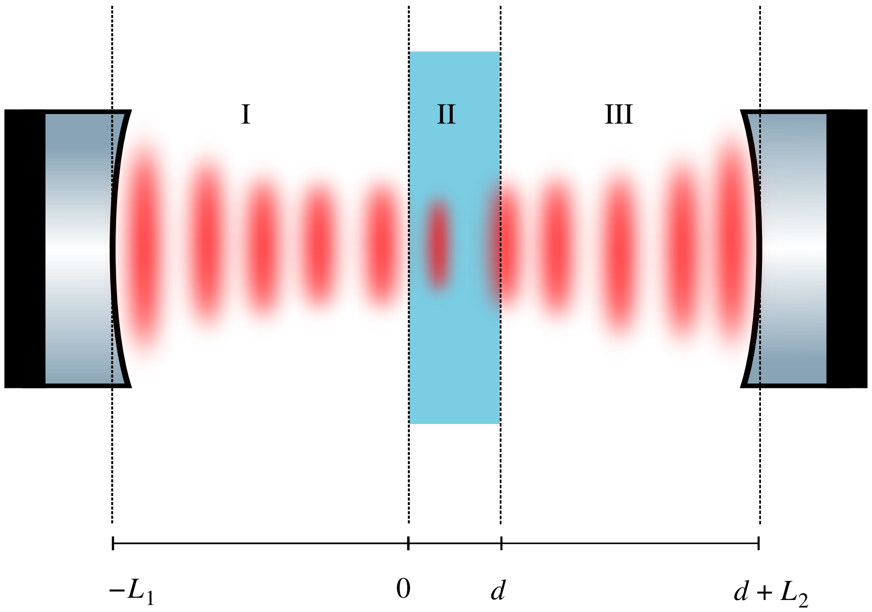

Figure 3.3: Membrane in the middle system with coordinate system with origin at the left membrane surface. A membrane with thickness d is placed in between a Fabry Pérot cavity, consisting of two concave mirrors with cavity length $L = L_1 + d + L_2$. The field inside the membrane (region II) is smaller (compared to regions I and III, filled with air), due to its higher refractive index.

One can construct the expected fields inside the cavity for a MIM system, by considering the boundary conditions. In figure 3.3 the MIM system for the field construction is sketched. The description assumes an ideal Fabry Pérot cavity, consisting of two mirrors with reflectivity of $R = 100\,\%$ and a membrane at the origin ($z = 0$) with thickness d and refractive index n. In this (coordinate) system mirror one is at position $-L_1$ (corresponding to the drum height) and mirror two is at the position $L_2 + d$ (see fig. 3.3). In this configuration, one can split up the cavity into 3 areas between membrane and mirrors (filled with air $n \approx 1$) and the membrane with thickness d itself. Neglecting losses and assuming a cavity length smaller than the Rayleigh length of the (Gaussian) beam [13], one gets the following plane wave ansatz for the fields (with the vector potential $\mathbf{A}$) in the three regions of the cavity (I-III) (see fig. 3.3):

$$\begin{aligned}
\mathbf{A}_I(z) &= \hat{A}_1 e^{ik_0 z} + \hat{B}_1 e^{-ik_0 z} \\
\mathbf{A}_{II}(z) &= \hat{A}_2 e^{ink_0 z} + \hat{B}_2 e^{-ink_0 z} \\
\mathbf{A}_{III}(z) &= \hat{A}_3 e^{ik_0 z} + \hat{B}_3 e^{-ik_0 z}
\end{aligned}$$

With the relations between the vector potential $\mathbf{A}$ and the electric ($\mathbf{E}$) and magnetic ($\mathbf{B}$) field [19]

$$\nabla \times \mathbf{A}(r,\omega) = \mathbf{B}(r,\omega) \qquad ; \qquad -i\omega\mathbf{A}(r,\omega) = \mathbf{E}(r,\omega)$$

one can construct the boundary conditions. For that one assumes a vanishing electric and magnetic field at the mirror surfaces and continuous magnetic and electric fields at the membrane surfaces. This then results in the following boundary conditions:

$$\begin{aligned} \mathbf{A}_I(-L_1) = \nabla\mathbf{A}_I(-L_1) = 0 \quad &, \quad \mathbf{A}_{III}(d+L_2) = \nabla\mathbf{A}_{III}(d+L_2) = 0 \\ \mathbf{A}_I(0) = \mathbf{A}_{II}(0) \quad &, \quad \nabla\mathbf{A}_I(0) = \nabla\mathbf{A}_{II}(0) \\ \mathbf{A}_{II}(d) = \mathbf{A}_{III}(d) \quad &, \quad \nabla\mathbf{A}_{II}(d) = \nabla\mathbf{A}_{III}(d) \end{aligned}$$

These boundary conditions then lead to a system of equations, with which the fields could be solved [2]. Further a transient equation can be constructed to develop a cavity resonance condition $R(d, L_1, L_2)$ for the set of system parameters (L_1, d, L_2) corresponding to the drum thickness, height and cavity length [13]:

$$R(d, L_1, L_2) = A_+(L_1)e^{-ink_0 d} - A_-(L_2)e^{ink_0 d}$$

with coefficients

$$A_\pm = \frac{1 \mp in \cdot \tan(k_0 L)}{1 \pm in \cdot \tan(k_0 L)}$$

A cavity resonance is reached for zero values of $R(d, L_1, L_2)$. The resulting resonance condition $|R_{min}|$ for varying values of L_1, L_2 is exemplary depicted in figure 3.4.

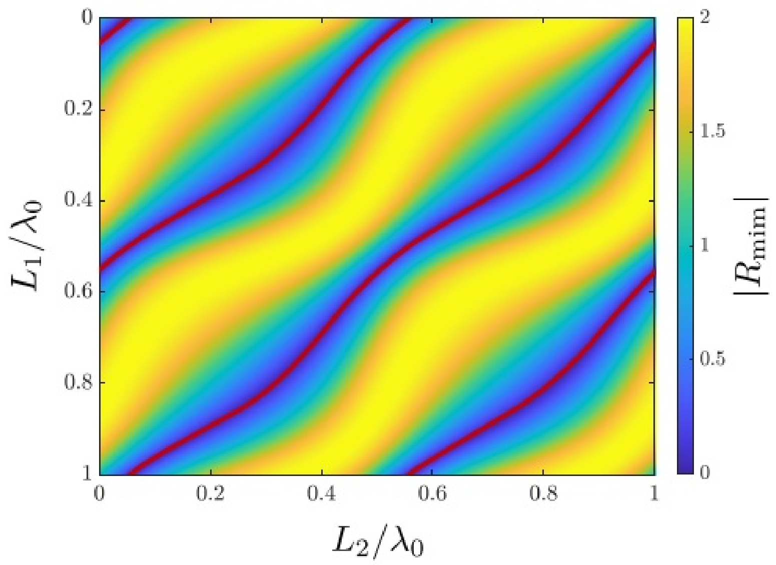

Figure 3.4: Cavity resonance condition for a fixed membrane thickness, (d = 1 µm, $n_{\mathrm{membrane}} \simeq 1.5$ [20]), plotted against L_1, L_2 and normalized to the laser wavelength λ_0 = 780 nm. The resonance condition is fulfilled for values of on the red line (taken from [13]).

[2] for the exact solution of the fields see [13]

With the resonance condition one can then simulate the coupling strength of the system in dependence of the drum parameter set (L_1, d, L_2). Considering a constant cavity length L_{cav} one scans the resonance condition for a variation of the laser frequency ($k_0 \pm \Delta k_0$) and the drum height ($L_1 + \Delta L$), as well as the length between drum and the second mirror ($L_2 - \Delta L$). From this, one can simulate the first order pullparameter (c.f. eq. (3.2)) for different cavity configurations (L_1, d, L_2), at which the resonance condition $R(d, L_1, L_2)$ becomes minimal. The resulting pullparameter $G^{(1)}$ for this MIM configuration is also exemplary mapped in figure 3.5 for different membrane thicknesses and drum heights $L_2 = L_{cav} - L_1 - d$ [13].

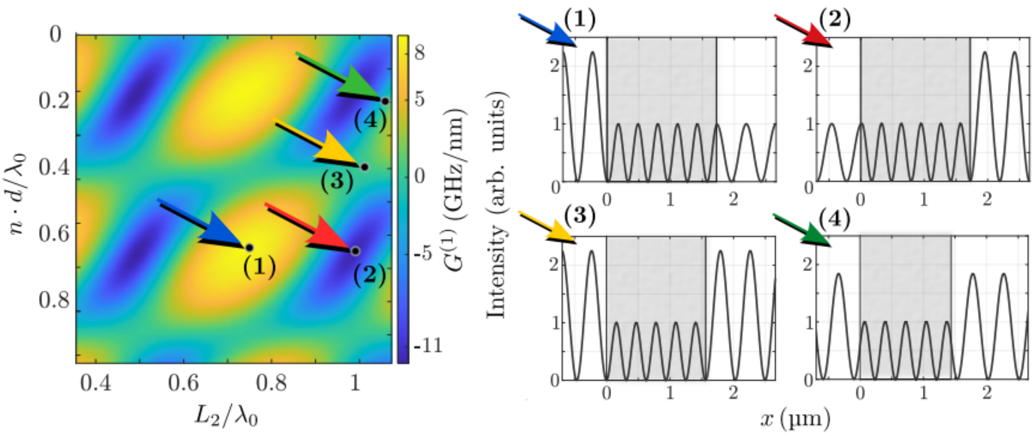

Figure 3.5: (Left) Map of the linear pullparameter $G^{(1)}$. The marked points on the map represent cases with different coupling strength (pullparameter) maxima or minima, due to the intensity configuration of the lightfield in the cavity (Right). A high intensity at the membrane boundary corresponds to a high coupling (cases (1) and (2)), while a low intensity at the boundaries corresponds to a low coupling (cases (3) and (4)); (taken from [13]).

The pullparamter in figure 3.5 shows an oscillatory behaviour with a period of one (material) wavelength λ_0/n. From this map one can derive the cavity configurations with higher and lower otpomechanical coupling, due to high or low intensity areas at the membrane surface, which is further depicted in figure 3.5. With the pullparameter and the zero point fluctuation x_{ZPF} (which can be derived from mechanical simulations of the membrane oscillations) the theoretical optomechanical coupling strength can be estimated (see eq. (3.7)). For the polymer drum MIM-systems, as used in this thesis, vacuum coupling strengths of $g_0/2\pi > 25\,\text{kHz}$ had been achieved [13, 11].

CHAPTER 4

Mechanical Properties of Polymer Drums

For the optomechanical experiments polymer drums were used, which were directly placed on the cavity mirrors by direct laser writing. Though these polymer drums show good optomechanical coupling, due to their viscoelastic nature these systems tend to have high mechanical losses, which limits their application. This chapter is therefore dedicated to give a brief explanation of the important mechanical characteristics to understand the mechanical and material properties of the membrane. Further, an overview of the selected drum design and the expected oscillatory behaviour, derived from finite element (FEM) simulations, will be given.

4.1 Dynamic Material Characteristics

A sinusoidally moving 3-dimensional mechanical oscillator, can be characterized by the stress and strain relations of its material. For an ideal elastic material, the main defining material properties for an elastic analysis are the young's modulus E (in Pa), the dimensionless poisson's ratio ν and the material density ρ. The young's modulus describes the deformation ϵ_0 of a material in relation to the applied stress σ_0 and corresponds to the spring constant of a one dimensional oscillator. For a sinusoidally moving material with frequency ω the time dependent stress and strains are given by[21]

$$\epsilon(t) = \epsilon_0 \sin(\omega t)$$
$$\sigma(t) = \sigma_0 \sin(\omega t + \delta)$$

where δ describes the phase shift between applied stress and material strain response (see fig. 4.1). For an ideal elastic material there is no phase shift ($\delta = 0^\circ$), while for an ideal viscous material the phase shift is $\delta = 90^\circ$ which leads to mechanical damping[21]. The poisson's ratio is a property that describes the ratio of width increase in xy-direction, of the 3-dimensional material, while decreasing in z-direction [21].

Since a material, like the used polymer, is in general not an ideal elastic material but rather viscoelastic, due to its viscous behaviour, it exhibits damping losses. To characterize these losses in the oscillating material, the young's modulus splits up into a real and an imaginary part. The real part, so called storage modulus E', characterizes the stored elastic energy and the imaginary part, the loss

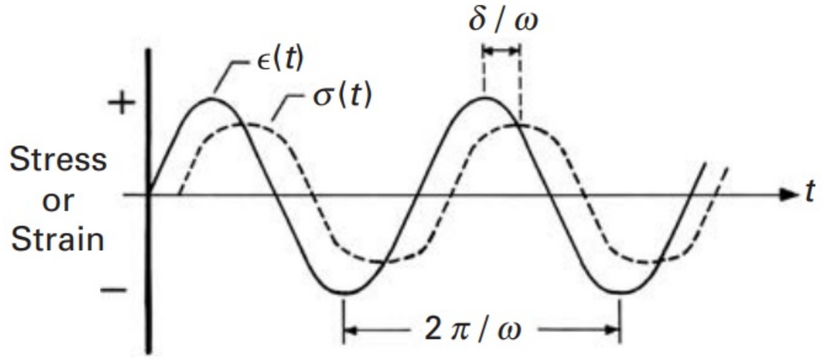

Figure 4.1: Phase relation between sinusoidally applied stress and resulting strain (taken from [21])

modulus E'', characterizes damping the losses. They are given by the phase dependent relations [21]

$$E' = \frac{\sigma_0}{\epsilon_0}\cos(\delta)$$
$$E'' = \frac{\sigma_0}{\epsilon_0}\sin(\delta)$$

and form the so called complex or dynamic young's modulus

$$E = E' + iE''$$

which becomes important in the simulation of the polymer drums oscillation (see sec. 4.4.1).

4.2 Thin Plates

The mechanical oscillations of the drums can be understood as those of a two dimensional membrane. Since an ideal membrane is 2-dimensional, a more realistic description of the used drum membranes can be given by thin plates, which also account for their finite thickness. With the bending theory of plates, developed by G.R. Kirchhoff and others in the 19th century [22], one can derive an equation of motion for the lateral displacement $w(x, y, t)$ of such a plate [22]

$$\nabla^2(\nabla^2)w(x, y, t) = -\frac{2\rho h}{D}\frac{\partial^2}{\partial t^2}w(x, y, t)$$

with the so called bending stiffness $D = \frac{2h^3 E}{3(1-\nu^2)}$, young's modulus E, plate thickness h and material density ρ. From this partial differential equation one can analytically derive the eigenmodes (displacement function $w_{mn}(x, y, t)$) with corresponding eigenfrequencies of a plate, depending on its geometries and boundary conditions [22]. The amplitude profiles of the first six independent vibrational modes are exemplary depicted in figure 4.2.

The analytical solution to this differential equation is rather complicated and not important for

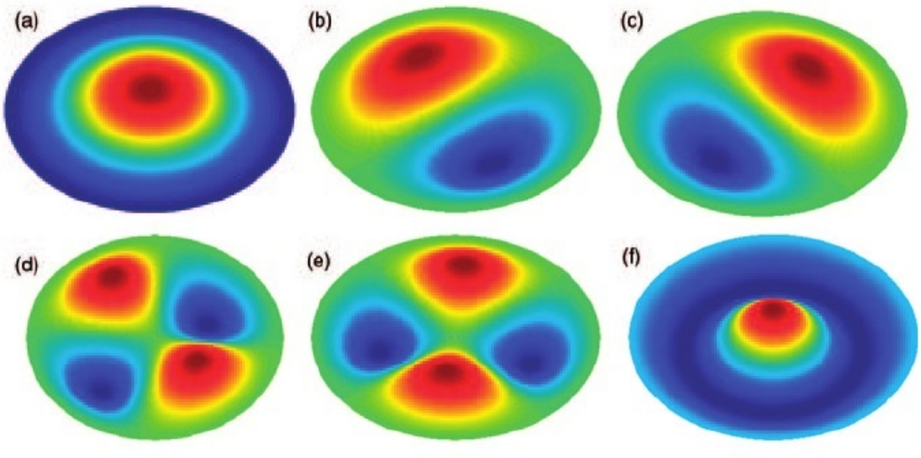

Figure 4.2: Simulations of the first 6 mode shapes for a fully clamped circular plate. (a) is the fundamental mode and (b)-(f) the next higher order modes (taken from [23])

this thesis[1]. However, to get an idea of the behaviour of the solutions, which will behave similar to the later used polymer membranes, the fundamental mode of a lossless circular plate, clamped at its boundaries, is given [22]:

$$\omega_{11} = \frac{10.33}{Radius^2}\sqrt{\frac{D}{\rho h}} \tag{4.1}$$

To get an idea of the actual oscillation behaviour and the corresponding resonance frequencies and linewidths, for the used polymer drum designs, numerical simulations were conducted (see section 4.4.1). To avoid confusions, the drum plates will be referred to as membranes in the following.

4.3 One dimensional Equation of Motion

For the optomechanical treatment it is convenient to describe the normal motion of a membrane (up and down) by a one dimensional oscillation. For each drum mode this then leads to the simplified and well known one dimensional equation of motion for a driven mechanical oscillator [5].

$$\ddot{x}(t) + \Gamma_m \dot{x}(t) + \Omega_m^2 x(t) = \frac{F_{\text{ext}}(t)}{m_{\text{eff}}} \tag{4.2}$$

m_{eff} describes the effective modal mass for a given mechanical mode of the membrane, $F_{\text{ext}}(t)$ describes the external force, Γ_m the dissipation rate and Ω_m the resonance frequency of the mode.

4.3.1 Mechanical Dissipation

For quantifying the performance of a mechanical oscillator and its losses, its quality factor Q plays an important role. Mechanical losses of an oscillator are then described by its dissipation rate Γ_m which

[1] For a more detailed description and solution of this equation see [22]

is defined by the mode frequency Ω_m and its quality factor Q (and vice versa) [5]:

$$\Gamma_m \simeq \frac{\Omega_m}{Q} \tag{4.3}$$

There are several reasons for dissipation losses in mechanical oscillators, especially for the used polymer membranes. One of the main reasons is viscous damping, caused by interaction with surrounding gas atoms or by compression of the viscous material layers. Another reason are clamping losses, which are caused by transversal oscillations along the membrane surface. Also anharmonic effects, like thermoelastic damping or phonon-phonon interaction, can lead to dissipation losses [24, 25]. The different dissipation effects further act independent of each other on the mechanical quality and cause a total mechanical quality Q_{tot}, given by [5]

$$\frac{1}{Q_{tot}} = \sum_i \frac{1}{Q_i} \tag{4.4}$$

The approach of layering the drums with a dielectric material, mainly aims to reduce the viscous damping losses, as well as clamping losses due to a harder membrane surface.

For optomechanical applications, the so called "$Q \cdot f$" product is an often used quantity to characterize the decoupling of the mechanical oscillator from a thermal environment (with $f = \Omega/2\pi$). With this quantity the number of coherent oscillations in presence of a thermal decoherence can be described [5]

$$\frac{\Omega_m}{\bar{n}_{th} \cdot \Gamma_m} = (Q \cdot f) \times \frac{\hbar}{k_B T} \tag{4.5}$$

with the average thermal phonon number $\bar{n}_{th}$, Boltzmann constant k_B and temperature T. From this the condition on the mechanical resonator for overcoming thermal decoherence is given by [5]:

$$Q \cdot f = \frac{Q \cdot \Omega_m}{2\pi} > \frac{k_B T}{\hbar} \tag{4.6}$$

4.4 Drum Design

Since this thesis is based on the work by L. Tenbrake *et al.* [11, 13] the drum designs have a similar shape, consisting of a circular membrane with outer diameter of $D = (66.0 \pm 0.3)$ µm supported by four circular posts with a width of $w = (3.0 \pm 0.3)$ µm (see fig. 4.3), with errors estimated from the limitations of the used printer [12]. Since the experiments were conducted in "free space", i.e. at room temperature and atmospheric pressure, the design further adapts the concept of a circular drum with several cuts inside the membrane [13] (see fig. 4.3). Compared to full circular drums, the cut ones should allow for a better movement of the membrane and less air resistance. Though both drum types were fabricated, in the experiments better results were achieved for samples with cut drum design rather than full drums, which is why they were preferred for the investigations of layered drums (see chapter 6).

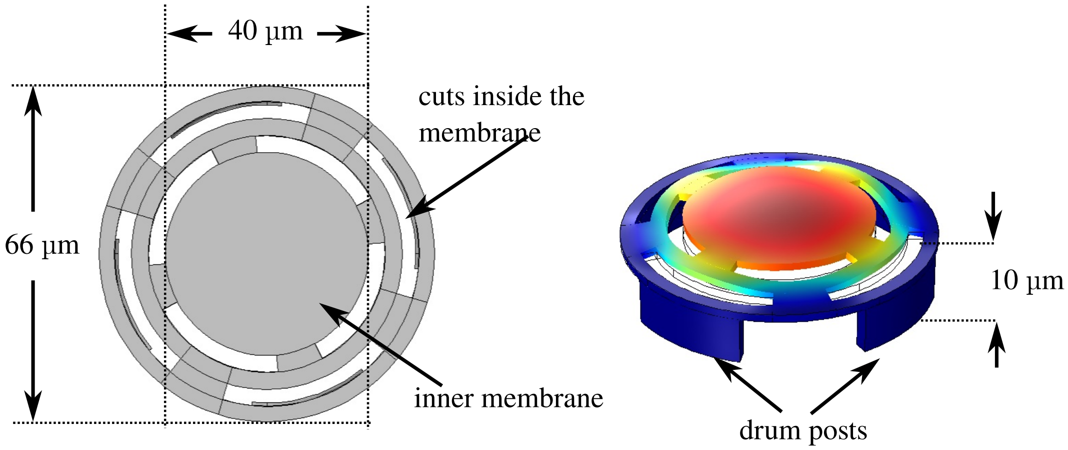

Figure 4.3: Drum design of circular drum with cuts the inside membrane. (Right) Simulation of the fundamental mechanical mode.

4.4.1 Simulations

The theoretical description of mechanical drums (as thin plates) give a good (first) understanding of the membrane dynamics, their application is though limited to certain geometries as well as special boundary conditions. For a sufficient analysis of the physical properties of the used drums, one relies on numerical simulations. For this, the solid mechanics module of the commercial software *COMSOL* was used to carry out an eigenmode analysis of the first oscillation modes. The software uses a finite element method (FEM), which splits up the entire geometry into a finite number of triangular elements in which the displacement and stresses are solved in each element of the geometry ([22, 26]).

An eigenmode analysis was conducted for an exemplary sample drum with the mentioned geometries above (see fig. 4.3) and a membrane thickness of 2.0 µm. From the simulations one can estimate the expected resonance frequencies of the fundamental mode $\Omega_m/2\pi$ as well as its linewidth $\Gamma_m/2\pi$. Further the effective mass for each mode can be derived from the simulations, by integrating the displacement field $\mathbf{u}(x, y, z)$ over the entire simulation volume V and the local density $\rho(x, y, z)$ [26, 13].

$$m_{\text{eff}} = \frac{\int_V dV \rho(x, y, z)(\mathbf{u}^T \mathbf{u})}{max_V(\mathbf{u}^T \mathbf{u})}$$

The value of the effective modal mass becomes important, if the zero point fluctuation x_{ZPF} of the membrane ground mode (see chapter 3) needs to be evaluated, which however won't be the case in the rest of this thesis.

For the simulations, the viscolelastic properties of the polymer material were used (IP-S; see sections 5.1, 5.3). The results for an exemplary polymer drum with a polymer thickness of 2.0 µm can be found in table 4.1. The simulations were conducted in vacuum, which neglects air resistance. Sources for the simulated loss rate Γ_m are therefore purely due to intrinsic damping losses, which is characterized by the loss modulus (E'') of the material. Since this thesis investigates the influence of deposited dielectric layers, the simulations were further conducted for various layer thickness of MgF_2 on top of the polymer membrane. The results are also listed in table 4.1.

Layer thickness [nm]	$\Omega_m/2\pi$ [MHz]	$\Gamma_m/2\pi$ [kHz]	m_{eff} [ng]	Q
0.0	0.787	22.31	4.41	35.28
100	1.073	24.38	5.1	44.01
150	1.101	25.96	5.3	42.41
200	1.118	26.88	5.7	41.59

Table 4.1: Mechanical parameters, from FEM simulations of the fundamental drum modes for a 2.0 µm thick polymer membrane with increasing layers of MgF_2.

From the simulations of the fundamental mechanical mode (in tab. 4.1) the resonance frequencies can be estimated for the following measurement, which should be around $\Omega_m/2\pi = 0.787$ MHz and gets shifted by each layer up to $\Omega_m/2\pi = 1.118$ MHz. The effective mass m_{eff} also gets shifted to higher values, which could negatively impact the optomechanical coupling, since g_0 is proportional to the zero point fluctuation $x_{ZPF} = \frac{\hbar}{\sqrt{2m_{\text{eff}}\Omega_m}}$. The simulations suggest a (relative) high increase of the qualities ($\Delta Q_{max} = +10$) by adding MgF_2 (100 nm) layers to the polymer, but still in a relatively low quality region. With view to the simulation results, this is mainly due to a sharp increase in resonance frequency for small layers, which saturates with each layer, and a rather small linear increase in linewidth (i.e. mechanical losses). From the simulations a small improvement of the mechanical quality can be expected, which is experimentally confirmed in chapter 6

Since the polymer membrane itself exhibits high mechanical losses, the possibility of entirely removing the polymer layer of a coated drum, beneath the dielectric layer, is also considered. Because such a removal would leave a comparably thin membrane ~ 100 nm, a more stable fully circular drum design is used for the simulations and the experiments (see fig. 4.4).

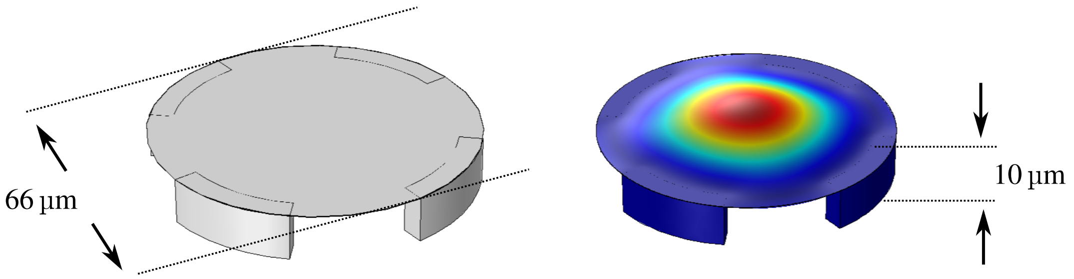

Figure 4.4: Drum design of full circular drum with membrane consisting of only 100 nm MgF_2 layer. (Right) Simulation of fundamental mechanical mode.

The simulation of the fundamental mechanical mode gives promising results. Though the resonance frequency $\Omega_m/2\pi = 0.336$ MHz is rather low compared to layered polymer membranes, it has a much smaller effective mass and should allow for much higher qualities of up to $Q \simeq 162$.

Layer thickness [nm]	$\Omega_m/2\pi$ [MHz]	$\Gamma_m/2\pi$ [kHz]	m_{eff} [ng]	Q
100	0.336	1.014	0.5	162.71

Table 4.2: Mechanical parameters, from FEM simulations of the fundamental drum modes for a bare 100 nm thick membrane of MgF_2.

CHAPTER **5**

Fabrication Methods

For the experiments polymer drums were directly placed on a distributed Bragg mirror (DBM) in a hybrid fiber Fabry Pérot cavity. The drums were fabricated with the commercial 3D printer *Photonics Professional GT+* by the company *NanoScribe*. The printer uses a technique called direct laser writing (DLW), which allows for a fast and precise way to create polymer drums in the µm-range for the MIM systems.

This chapter is dedicated to introduce to the fabrication methods used, as well as discussing the individual fabrication steps and possible error sources.

5.1 *NanoScribe*

The drums were fabricated with the *NanoScribe Photonics Professional GT+* (see fig. 5.1 left), which is a commercially used 3D-Printer[1]. The printer is one of the main tools for the drum fabrication, which is why the printer and its properties are briefly described here. For a more detailed description of the system and its usage see [12, 27].

Its printing method is laser lithography, also called direct laser writing (DLW), which is used to produce precise three dimensional structures from a few millimeter to sub-micrometer range. The printer consist of a pulsed femtosecond laser with a wavelength of 780 nm and a power of 50 mW [27]. It operates with two photon absorption to polymerize a photo resist at the desired coordinates. This enables the laser to write structures only in the beam focus without hardening the resist in the beam path, as is depicted in figure 5.1 on the right side.

Photo Resist The photo resist used for the drums, is called IP-S and is a negative tone resist by *NanoScribe* used for the fabrication of relatively small and smooth structures. It gets polymerized by absorption of a photon with $\lambda = 390\,\mathrm{nm}$, which is double the energy of the $\lambda = 780\,\mathrm{nm}$ laser of the printer. It has refractive index of $n_{ips}(780\,\mathrm{nm}) = 1.51$ [12, 20], a density of $\sim 1.2\,\mathrm{g/cm^3}$, a complex young's modulus of $(5.33 + i0.26)$ GPa and a poisson's ratio of 0.3 [12, 28, 29, 30].

Writing Modes The *NanoScribe* system can choose between 3 different types of writing modes. In the *StageScanMode*, the motorized (substrate-) stage is directly moved, relative to the laser beam,

[1] Nanoscribe GmbH :`https://www.nanoscribe.com/de`

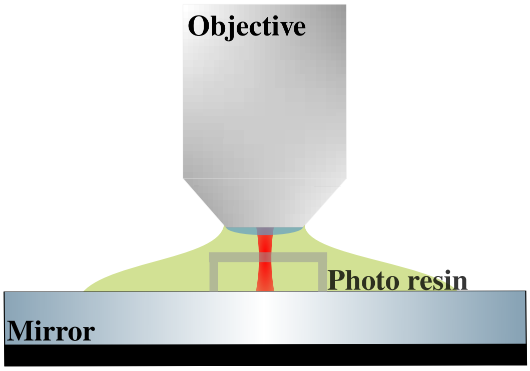

Figure 5.1: (Left) The 3D printer *NanoScribe Photonics Professional GT* [27]. (Right) Concept of direct laserwriting in DiLL configuration. The photo resin gets polymerized only in the beam focus.

allowing for writing at the desired coordinates (in the xy-plane). With this writing mode rather large structures (~mm) are written at the expense of precision. The second mode with a smaller writing field, is the *PiezoScanMode*, which moves the stage by its piezo drive and is used for very fine and small structures ($< 200\,\mu m$). The last one, the *GalvoScanMode*, uses a galvomirror to redirect the laser beam to the coordinates, and is used for intermediate sized structures with less precision than the *PiezoScanMode*. For printing in z-direction the objective further consists of a motorized as well as a piezo driven z-drive [27].

Writing Parameters For a well printed structure, it is important to adjust the writing parameters. The two main parameters, which need to be adjusted, are the *ScanSpeed* of the laser (in µm/s) and the *LaserPower* (in %). An increase in the laserpower for example results in less exposure of the photoresist, which then requires a higher *LaserPower*. The combination of the two parameters defines the also called "*dose*". A wrong choice of these parameters can result in badly polymerized structures due to underexposure, or evaporation of the resist and bubbles forming in the structure due to overexposure [31]. It is therefore always recommended to conduct such a "*dosetest*", in which several test structures are printed with a parameter sweep, before printing the actual structures.

Writing Configuration The printer focuses the laser beam through an objective inside a drop of photo resist on a glass substrate. For this the printer can be used in three different writing configurations (see fig. 5.2). The first two configurations approach the substrate from beneath and focus the beam through the glass onto the photo resist. In the first configuration, called air configuration, air is used as immersion medium between objective and glass substrate. The second one is called oil immersion configuration and uses oil as immersion medium. The last one, which is the one used for the fabrication, is the so called Dip-in-Laser-Lithography (DiLL) configuration. The Objective is "dipped" directly in the photoresist from above and uses it as immersion medium. This allows for a better focus of the laser inside the resist and also for higher structures due to fewer height limitation of the objective.

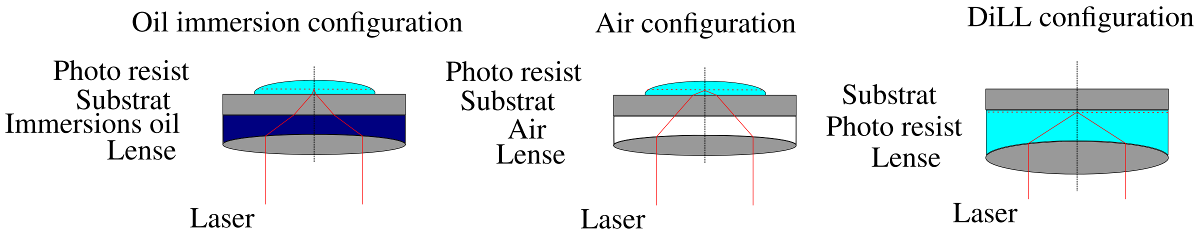

Figure 5.2: Examplary depiction of the three possible writing configurations in *NanoScribe*. (Left) The oil immersion configuration uses oil as immersion medium for a better focus. (Middle) In the air configuration, the laser is focused through air. (Right) In the dip in laserlithography (DiLL) the objective is directly dipped in the photo resist and uses it as immersion medium [27, 32].

5.2 Drum Fabrication

For the main production of the drums I used the *PiezoScanMode* for most of the samples. In combination with the photoresist this mode is best suited for producing high quality structures with smooth surfaces [12], which is important for a transparent membrane with low scattering losses. Further, the piezo writing field of 200 µm × 200 µm allows for printing the entire drum geometries (diameter ~ 70 µm) without rearranging the stage.

For all drums the DiLL configuration was used, which allows for less diffraction errors of the laser and in particular less limitation in the height of the structure. Before starting to fabricate the drums, a few dosetests for the drum structures (in galvo and piezo in scan mode) were conducted to find the best suited writing parameters. The drum posts are not hard to produce. They are solid and have a wider range of suitable writing parameters. To avoid damages of the piezo in *PiezoScanMode*, the *ScanSpeed* is usually held below 400 µm/s, which results in a rather long writing time of the posts. The membranes on the other hand are rather thin free hanging structures, especially during the printing process, which is why their writing parameters are the more difficult to find. In the *PiezoScanMode*, as a compromise between writing time and good quality, a *ScanSpeed* of 100 µm/s with a *LaserPower* of 39 % was used for the membranes and for the solid posts a *ScanSpeed* of 200 µm/s with a *LaserPower* of 45 %. An example of a printed drum, together with the programmed coordinates is depicted in figure 5.3. The finished structures after development are depicted in figure 5.4.

5.2.1 Possible Error Sources

Since the beam shape of the laser during the writing process is limited by the numerical aperture and magnification of the objective, the thickness of the membranes is limited to ~ 1 µm for a single written layer [12]. Due to variations of the writing parameters and proximity effects while printing in the photoresist, the actual size of the drum will differ from the programmed geometries [12]. This especially effects the desired membrane thickness of a drum. To account for the finite lateral size of a polymerized line, during the printing process, the written coordinates are partially corrected. According to *NanoScribe* [12] the used objective (63x, NA 1.4) has a lateral beam size of ~ 0.8 µm. For a partial correction of this effect, the programmed coordinates for a desired membrane thickness are therefore reduced by ~ 0.8 µm. Due to the variations of the beam shape, during the printing process, the actual size can still only be estimated.

Another possible error that can occur are ripped membranes (see fig. 5.5). Due to the thin nature

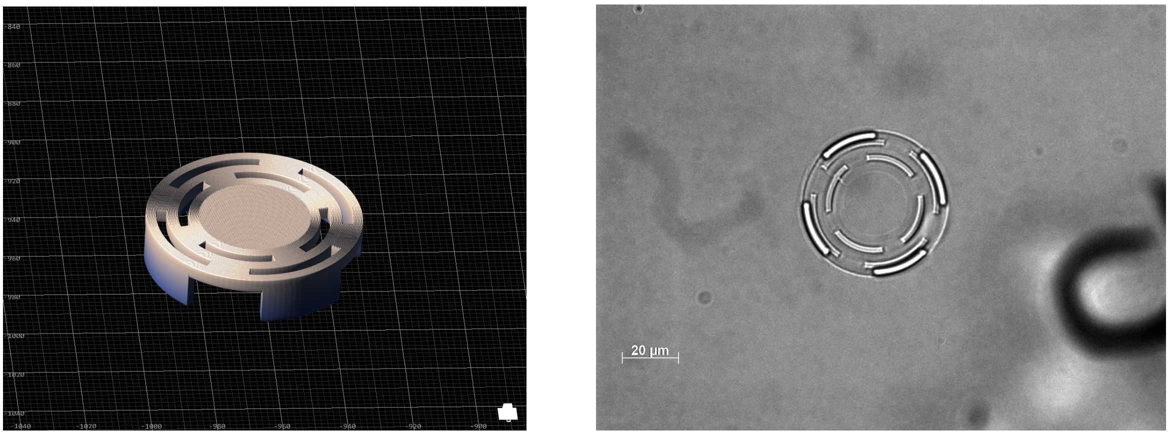

Figure 5.3: (Left) Programmed structure, depicted in the *NanoScribe* editor (*DeScribe*) [27]. (Right) The finished structure in the printer.

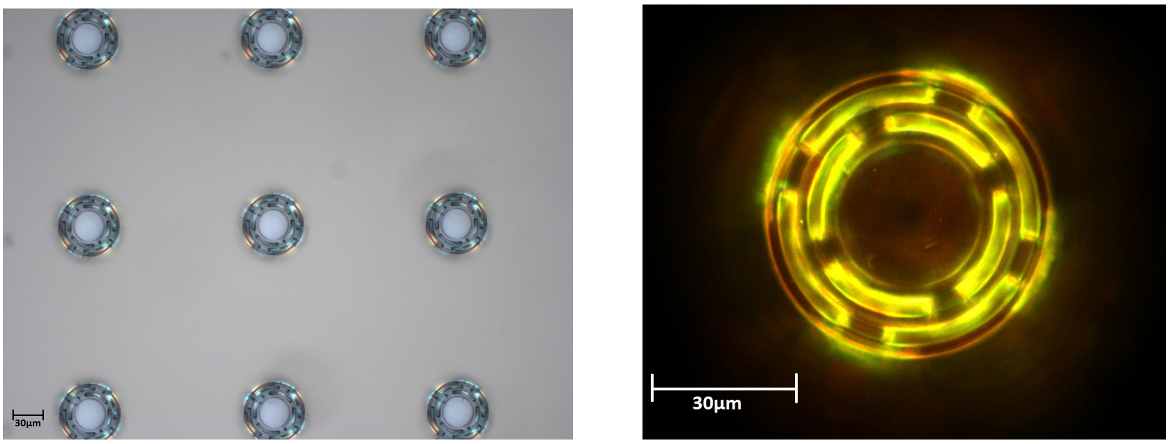

Figure 5.4: Drum structures after development in the optical microscope. (Left) Excerpt of drum array for measurement. (Right) Close up of a drum sample in dark field.

of these membranes (~ 1 µm) compared to their diameter (~ 60 µm), pressure on the membranes during the printing process, by movements of the photoresist or evaporation during the development process with isopropanol[2], can lead to this problem. This turned out to become important in the last experiments (see chapter 6), when trying to reduce the polymer layer. This problem can be reduced by either using lower *ScanSpeeds* in *PiezoScanmode* or by using the *GalvoScanmode* (with 15 000 µm/s speed and 96 % power) on the expense of the surface quality of the membrane.

[2] For developing the structures after the printing process, the unpolymerized photoresist needs to be removed in a development process (see [27])

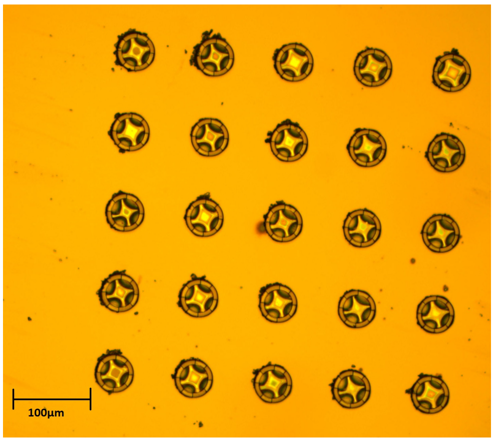

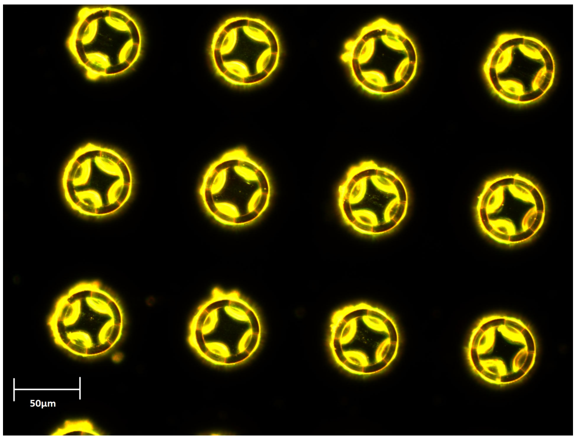

Figure 5.5: (Left) Optical microscope image of ripped membranes after printing process. (Right) Closeup of ripped membranes in dark field

Plasma Etching The hardened polymer can be post processed by an air plasma treatment in a plasma oven[3], to get rid of small pollutions on the structures and also to achieve a polishing effect on the surfaces of the drum. A longer plasma process can further be used to edge off the polymer, thereby reducing the drum thickness (see section 6.3).

5.3 MgF_2 Layer Deposition

For the layer deposition a thermal evaporation machine was used, which uses a current to heat up a tungsten crucible (also referred to as boat) to evaporate MgF_2 crystals inside (see fig. 5.6).

During the evaporation process cracks can occur inside the deposited MgF_2 layer on the drums, as depicted in figure 5.7. The thicker the layer the more likely is the occurrence of such cracks across the membrane. For small cracks an optomechanical response can still be detected. For larger ones, optical scattering losses, as well as mechanical losses become too high for a measurable response. The main reason for the formation of these cracks is the different temperature of the polymer surface and the comparably hot deposited layer of MgF_2 with different expansion coefficient ([12, 33]), which results in surface tensions while cooling down. Another main reason for the formation of cracks is the surface roughness of the polymer drums, which can also lead to micro cracks in the MgF_2 layer while cooling down[34, 35].

To avoid such cracks in the evaporation process, prior to the layer deposition the drum surfaces are treated with a short plasma etching process (5 minutes at 55 %) to reduce a possible surface roughness of the polymer and hence reduce the risk of cracks. The process further helps to reduce scattering losses due to a rough polymer surface [13]. Further, only comparably thin layers (≤ 50 nm) were deposited in a single evaporation run to avoid too much tension in the layer, while evaporating. With both measures the formation of cracks could be reduced to an acceptable level for layer-thicknesses of up to 150 nm, after which cracks couldn't be avoided in the fabrication.

[3] Diener electronic GmbH: `https://www.plasma.com`

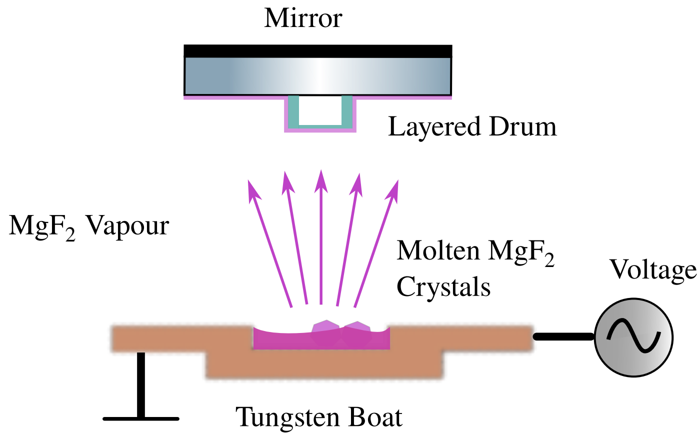

Figure 5.6: Schematic depiction of thermal evaporation process.

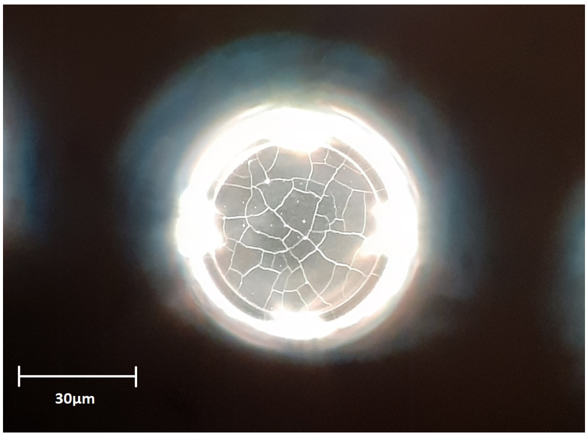

Figure 5.7: Darkfield image of cracks inside the evaporated MgF_2 layer on a fully circular test drum.

Magnesium fluoride (MgF_2) The main material, used for the layer deposition and investigation in the experiments, was magnesium fluoride (MgF_2). It is an inorganic compound (a salt) and can be found as white dust or as a colorless crystal (with tetragonal crystal structure). MgF_2 has a refractive index of $n \approx 1.38$ and a high transmission in the visible optical spectrum [33], which is why it is often used in optical components (e.g. mirrors) as coating. It has a density of $3.18\,\mathrm{g/cm^3}$, a young's modulus of $E = 135.8\,\mathrm{GPa} + i0.25\,\mathrm{GPa}$ (loss modulus estimated from [36]) and a poisson's ratio of $\nu = 0.278$. It is well suited for the experiments, because of its low loss optical properties in the visible to infrared region and especially its rather high elastic properties, like its ~ 25 times higher young's modulus compared to the used polymer (IP-S)[12, 33]. Magnesium fluoride was further primarily used for the experiments, because it is one of few dielectric materials for which thermal evaporation is recommended [37].

CHAPTER 6

Measurements

The polymer membranes used for the optomechanical MIM systems, as mentioned before, show comparably high dissipative losses due to their viscous nature. This has a big influence on the mechanical quality of the oscillators of the system. A high mechanical quality is desired, especially if quantum effects like strong coupling or side band resolved cooling are investigated, for which the thermal decoherence rate of the system needs to be much smaller than its optomechanical couplingstrength [5].

To improve the mechanical quality at room temperature and atmospheric pressure, a layer of a transparent dielectric material with better mechanical properties than the polymer is deposited on the membrane. The higher young's modulus of the dielectric material (here MgF_2) is supposed to stiffen the membrane and therefore improve the mechanical oscillation properties and increase the mechanical quality.

This chapter presents how the layered drums were tested for their optomechanical response and their associated mechanical oscillation properties. The influence of layer deposition on the polymer drums is discussed. Further this chapter discusses the effect of a potential removal of the polymer beneath the dielectric layer.

6.1 Experimental Setup

For investigating the optomechanical responses of the membranes the probe beam setup, sketched in figure 6.1, was used. As stated above, it is a variation of the optical setup, used by Lukas Tenbrake [13].

In the setup a wavelength tunable diode laser with a center wavelength of $\lambda_0 = 780\,\text{nm}$ and a power of $10\,\text{mW}$ was used as a probe beam. The linear polarized beam first passes a half-waveplate and is then sent through a polarizing beamsplitter (PBS), such that roughly half of the beam is transmitted and the other half reflected and blocked out (see fig. 6.1), mainly just to control the initial beam intensity. The (s-polarized) transmitted part then gets circular polarized by a quater-waveplate and then coupled (via a free space coupler) into the fiber cavity, where it gets reflected and coupled out again. The outcoupled beam then gets again linear polarized by passing the quater-waveplate in opposite direction and turned by the second half-waveplate, such that the beam has the polarization (p-polarization) to get fully reflected at the PBS onto the photo diode (PD) (see fig. 6.1). The diode signal (reflection signal) is then split up into DC (direct current) and RF (radio frequency or alternate

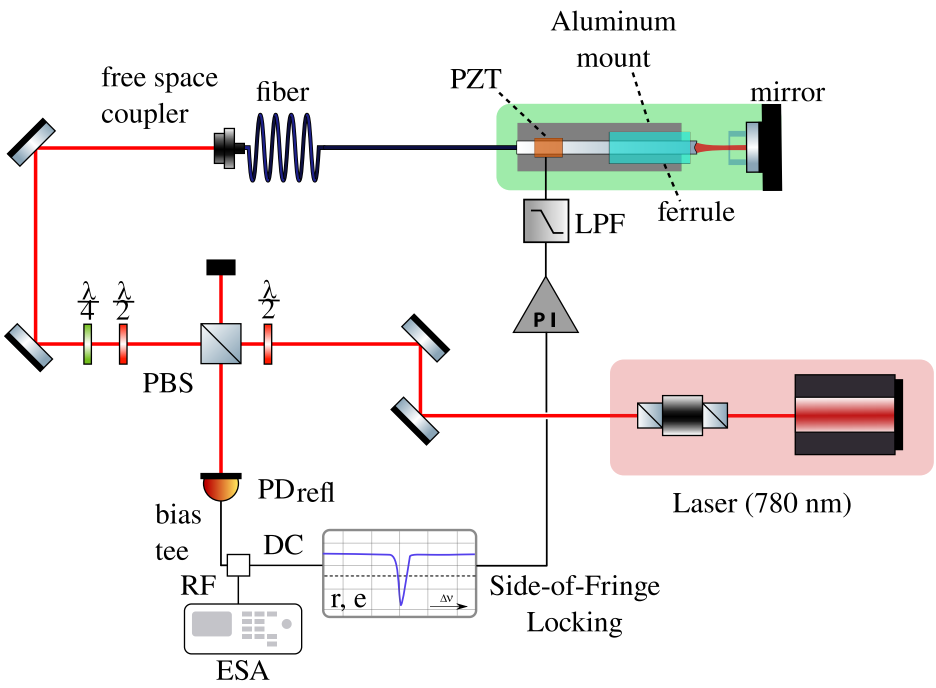

Figure 6.1: Probe beam setup for measuring the optomechanical response [13]. The laser beam gets coupled into the fiber cavity and gets reflected back onto a photodiode. The reflection signal (DC part) is used as error signal to lock the cavity with a PI-feedback loop. Further an optional low pass filter (LPF) can be used to reduce electronic noise. The membrane movements cause noise on the diode signal, which can be analysed on an ESA (RF part).

current) part by a bias tee. The RF part of the signal is sent to an electric spectrum analyzer (ESA), which displays the power spectral density (PSD) of the reflection signal. The DC part is used as error signal to lock the cavity by a PI-feedback loop controlling the piezo electric transducer (PZT) of the cavity. For the lock itself, a side of fringe locking technique was used (see section 6.1.2).

For measuring the optomechanical response the power spectral density of the reflection signal of the locked cavity is analyzed at the spectrum analyzer. Since the drums interact with the thermal environment, they will always slightly oscillate due to random thermal forces pushing on the membrane. This membrane movement causes noise on the reflection signal. This noise can be made visible by analysing the RF signal of the locked cavity on the ESA, which uses a fast fourier transformation to decompose the noise signal into its frequency components. The noise, caused by the drums, is then visible as noise on the power spectral density in form of Lorentzian curves for the drum modes at their respective resonance frequencies.

6.1.1 Noise on Power Spectral Density

For extracting the optomechanical parameters from the power spectral density (PSD), first a mathematical model of the PSD needs to be derived, which is only briefly discussed in this section. For a more detailed description see for example [5, 38, 39]

Starting from the well-known Wiener-Khinchin theorem, the power spectral density $S_{xx}(\Omega)$ can be connected to the auto correlation function $\langle X(t)X(0)\rangle$ by a fourier transformation[5]

$$S_{xx}(\Omega) = \int_{-\infty}^{+\infty} dte^{i\Omega t}\langle X(t)X(0)\rangle$$

The auto correlation function in general describes a correlation of a (random) signal with itself at different times [13]. To get the specific power spectral density corresponding to the position (signal/noise) of the membrane $x(t)$, the solution of the equation of motion (see eq. (4.2)) in frequency space is used. For a damped mechanical oscillator driven by an external force $F_{\text{ext}}(\omega)$ this then reads [5]

$$x(\omega) = \chi_{xx}(\omega)F_{\text{ext}}(\omega)$$

with the introduced susceptibility $\chi_{xx}(\omega)$:

$$\chi_{xx}(\omega) = [m_{\text{eff}}(\Omega_m - \Omega) - im_{\text{eff}}\Gamma_m\Omega]^{-1}$$

In thermal equilibrium, one can now bring the noise on the power spectral density (PSD) in relation to the dissipative part of the linear mechanical response over the Fluctuation dissipation theorem [38]. The noise on the PSD then reads

$$\begin{aligned} S_{xx}(\Omega) &= \frac{2k_BT}{\Omega} Im\{\chi_{xx}(\Omega)\} \\ &= \frac{2k_BT}{\Omega}\frac{1}{(\Omega^2-\Omega_m^2)^2+\Gamma_m^2\Omega^2} \end{aligned} \tag{6.1}$$

This formulation of the PSD (given in W/Hz) now corresponds to the noise fluctuations, sensitive to the positional movement of the membrane. However, since the ESA is sensitive to frequency noise on the cavity, rather than the membrane position, this formulation of the PSD needs to be adjusted [13]. By multiplying with the linear shift of the cavity frequency (i.e. the linear pullparameter $G = \frac{\partial\omega}{\partial x}$) the frequency sensitive form of the PSD ($S_{\omega\omega}$) is given by [39]:

$$\begin{aligned} S_{\omega\omega}(\Omega) &= G^2 \cdot 2S_{xx}(\Omega) \\ &= \frac{2g_0^2\Omega_m}{\hbar}\frac{2k_BT}{\omega}\frac{1}{(\omega^2-\Omega_m^2)^2+\Gamma_m^2\omega^2} \end{aligned} \tag{6.2}$$

This is the final form and proportional to the vacuum coupling strength g_0^2. Using this form, the mechanical properties can be extracted from the Lorentzian curves forming in the PSD signal.

6.1.2 Side-of-Fringe-Locking

For locking the cavity in resonance with the incoupled light field, a side-of-fringe method is used. This locking scheme is rather simple, yet it allows for a relatively stable locking of the cavity. Its basic operational principle is briefly described in this section.

By applying a ramp signal to the PZT of the fiber, the cavity gets scanned and its resonance curves can be displayed on an oscilloscope. The appearing cavity dips of the reflection signal are then used as reference for the lock. To create the error signal the reflection signal gets corrected by a constant value, such that the level of the side of the resonance fringe (point with steepest slope) is set to the zero crossing (see schematic depiction in figure 6.2).

A small change of cavity length or laser frequency then results in a swift de- or increase of the signal and therefore a change of the error signal in positive or negative direction. This can then be corrected by a PI-feedback loop to the PZT (see fig. 6.1), such that the error signal is constantly set back to the setpoint, which then effectively locks the cavity in resonance [40].

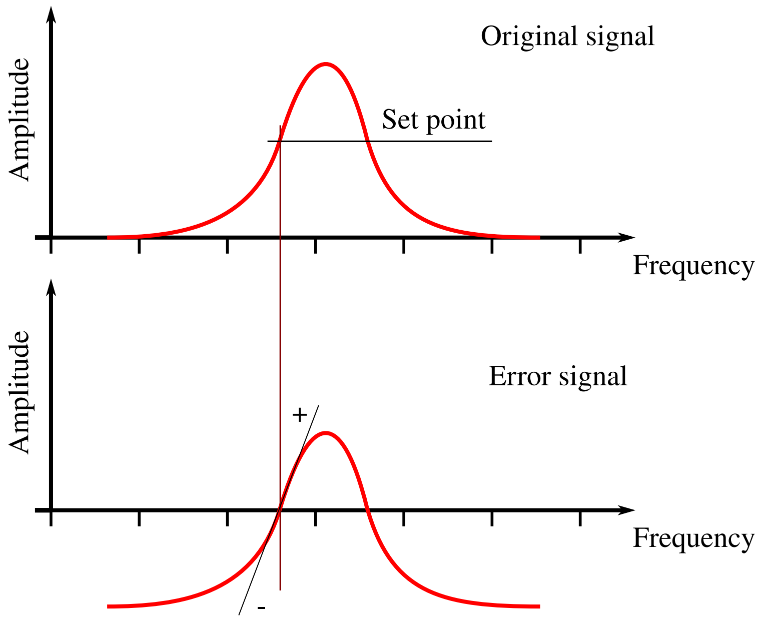

Figure 6.2: Schematic depiction of side-of-fringe locking scheme: A constant value can be added or subtracted to a resonance curve, to create an error signal for locking a cavity. The set point gets set to zero such that a signal increase or decrease result in a positive or negative change of the signal, which can then be corrected (varied from [40])

A more advanced locking technique, like the pound-drever-hall (PDH) technique, could also be applied to achieve a more stable lock [13, 41]. This on the other hand would require a more complicated setup, and for the purposes of the measurements in this thesis, the side-of-fringe method was sufficient enough.

6.2 Influence of Dielectric Layers

By depositing a layer of a dielectric material on top of the direct laser written polymer drums, the mechanical properties are expected to change. The effect was quantitatively measured for the fabricated membrane in the middle systems and the results are discussed in this section.

6.2.1 Measuring Procedure

For the measurement of the layer influence, the setup shown in figure 6.1 was used. To measure a drum, first a cavity with length of $L_{cav} = (30 \pm 5)$ µm between fiber and end mirror (with the desired drum in between) is created. The resonance curves can then be extracted from the measured PSD signal on the ESA after locking the cavity. For a stable cavity lock, as well as for a good signal on the ESA, a prominent cavity resonance signal, i.e. the depth of the resonance dip, is important. A signal improvement can be achieved by slightly scanning the laser frequency. Another possibility is by repositioning the fiber over the drum, since the thickness of the polymer could vary across the membrane, due to printing imperfections.

For the analysis of the layer influence the mechanical properties of the fabricated sample drums (see fig. 6.4) are measured. These measurements are then repeated after coating the drums with several 50 nm thick MgF_2 layers. The measured PSD signal on the ESA, from which the mechanical parameters are extracted, is exemplary depicted in figure 6.3 for one of the measured drums.

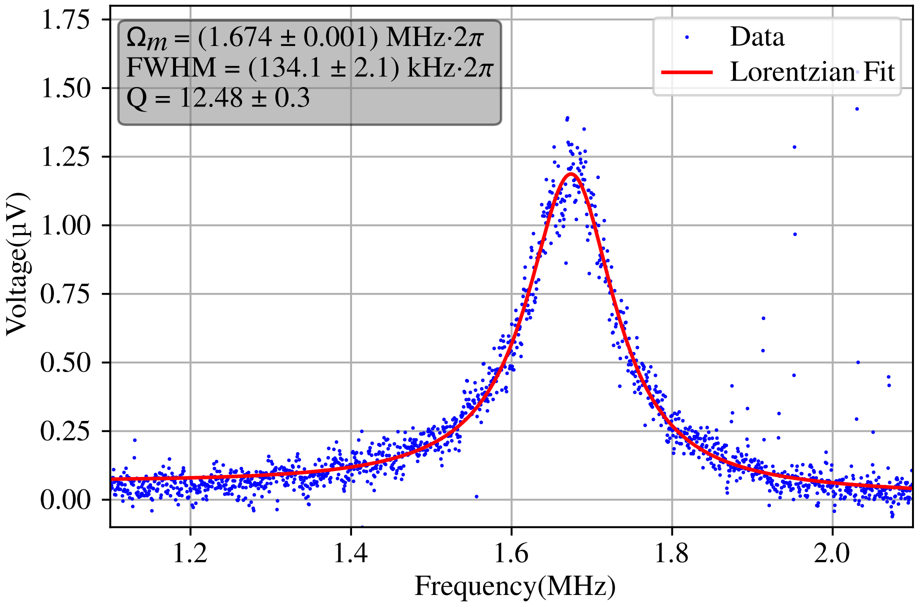

Figure 6.3: PSD signal of the fundamental mode of a layered polymer drum with 1.7 µm thickness and 10.0 µm height. From the Lorentzian fit the mechanical resonance frequency Ω_m and the linewidth (FWHM) can be derived.

The interesting mechanical parameters, evaluated from the resonance curves, are the resonance frequency Ω_m and linewidth of each mode, which characterize the mechanical performance. To extract those parameters from the measured noise signal on the PSD (see section 6.1.1), a Lorentzian curve was fit to the data according to the PSD noise model derived in equation (6.2). The linewidth is then given by its full width at half maximum (FWHM) which becomes:

$$FWHM \overset{\Omega_0 >> \Gamma}{\approx} \Gamma \tag{6.3}$$

The quality factor is then given by

$$Q = \frac{\Omega_0}{FWHM} \approx \frac{\Omega_0}{\Gamma} \tag{6.4}$$

6.2.2 Concept of Measurements

For a quantitative analysis of the effect of deposited dielectric layers, drums with 5 different membrane thicknesses, increasing from 1.7 µm to 2.1 µm in 0.1 µm steps, were fabricated. To also account for production variations and errors, 5 copies of each drum thickness were fabricated, which then results in a measurement array of a total of 25 drums (see tab. 6.1), for which the resonances were measured (see. 6.4).

1.7 µm	1.8 µm	1.9 µm	2.0 µm	2.1 µm
1.7 µm	1.8 µm	1.9 µm	2.0 µm	2.1 µm
1.7 µm	1.8 µm	1.9 µm	2.0 µm	2.1 µm
1.7 µm	1.8 µm	1.9 µm	2.0 µm	2.1 µm
1.7 µm	1.8 µm	1.9 µm	2.0 µm	2.1 µm

Table 6.1: Distribution of the polymer membrane thicknesses for the measurement array in figure 6.4. The fabricated thicknesses vary from 1.7 µm to 2.1 µm in 0.1 µm steps with 5 drum exemplars for each thickness.

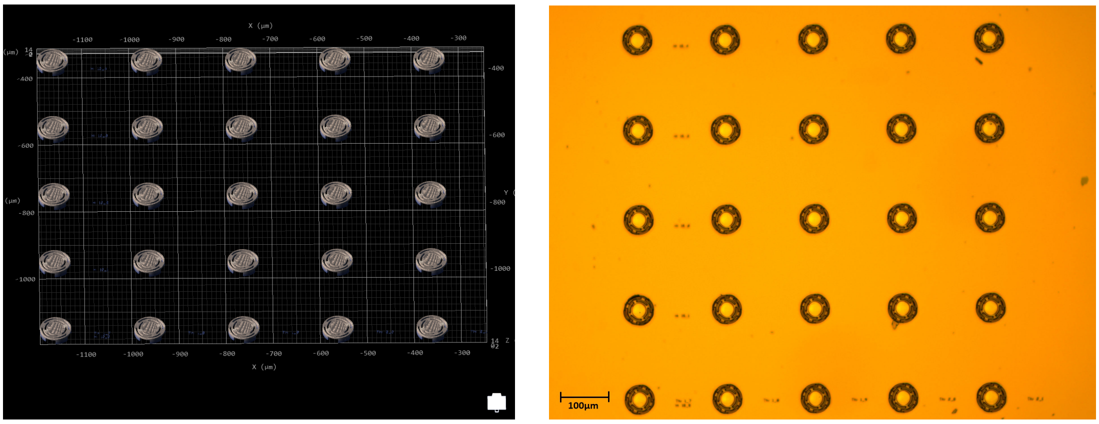

Figure 6.4: Array of the measured drums with cut design with big diameter of 60 µm (without counting the 3 µm thick posts) and small diameter of 40 µm. (Left) The programmed array in *DeScribe* [27]. (Right) Optical microscope picture of the printed samples.

The resonance parameters (Ω_m, Γ_m and Q) for all 25 drums, before and after evaporating each layer, were measured. For the layering part, three consecutive 50 nm MgF_2 layers were used (leading to a final thickness of 150 nm). With this a total number of 4×25 single measurements of the drums were conducted for this analysis. Since there were 5 drum samples for each polymer membrane thickness (see tab. 6.1), the average values of the extracted parameters over all 5 drums were taken, to have quantitative data for the overall effect of the layers on the membranes.

6.2.3 Results

In figure 6.5 the effect of a dielectric layer (100 nm MgF_2) on the signal of a single test drum can be observed for example. The bare polymer membranes exhibit resonance frequencies of around $\Omega_m/2\pi = 1.56$ MHz with rather small quality of $Q \simeq 11.6$. The comparison of both plots in figure 6.5 suggests a decrease in linewidth and an increase in quality. But also the opposite case was observed, in which the unlayered drum shows better mechanical properties. As stated above, to get a reliable picture of the overall effect the measurements for each run were conducted on 5 specimen, each fabricated in the same way, for 5 different polymer membrane thicknesses (25 measurements per dielectric layer). The development of the resonance frequencies for all measured drums is plotted in figure 6.6 against

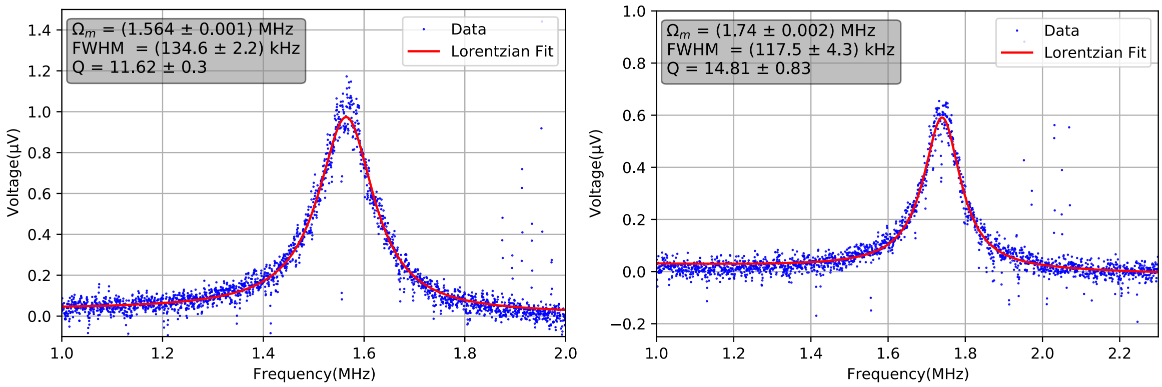

Figure 6.5: PSD signals of the fundamental mode of a polymer drum with 1.8 µm thickness and 10.0 µm height. (Left) Without dielectric layer. (Right) with 100 nm MgF_2 layer.

the polymer membrane thickness of the drums. Each data point represents the average of 5 samples with the same membrane thickness for the measured frequencies. With increasing thickness of the bare polymer membrane, the resonance frequency gains a noticeable but small shift. The shift is almost linear with with increasing thickness, except for the 2.1 µm membrane. This jump is most likely due to an error in the programmed coordinates for the 3D printer, which probably increased the coordinates (thickness) by 0.4 µm. The linear resonance shift is expected, since a thicker membrane causes a higher bending stiffness, which results in a faster oscillation and therefore a higher resonance frequency (c.f. eq. 4.1). The data for the increasing MgF_2 layers further show a comparably big shift of the average resonance frequency to higher values (up to $\Omega_m/2\pi = 1.75$ MHz) for each deposited layer. The first layer of 50 nm causes the biggest shift (~ 0.1 MHz), while for each following layer this shift apparently saturates. This "big" resonance shift, caused by the MgF_2 layers, is due to the fact, that the higher young's modulus of the layer increases the overall young's modulus of the then layered membrane and therefore its resonance frequency (c.f. eq. (4.1)).

Further, figure 6.7 shows the effect on the mechanical quality of the drums. Similar to the resonance frequencies, the overall quality factor of the drums increase slightly with each deposited layer. For the bare drums the overall qualities vary between 11.6 and 16. From the data in figure 6.7, overall quality improvements (up to $\Delta Q \simeq +4.2$) could be reached for most of the drums. This effect is mainly due to the shift in resonance frequency (see eq. (6.4)), since the average linewidths don't show a significant improvement per layer (see fig. 6.8). Due to imperfections at the interface of the polymer and dielectric layer and the finite loss modulus of MgF_2 (see sec. 5.2), the linewidths (losses) should rather increase with each layer. However, a clear trend can't be observed in figure 6.8.

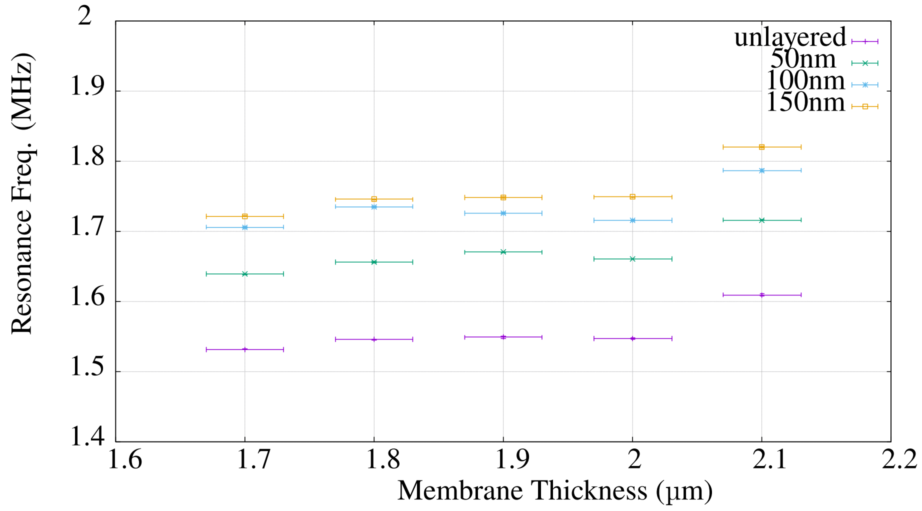

Figure 6.6: Development of the measured resonance frequency for different polymer membrane thicknesses and dielectric layer thicknesses. The errors on the membrane thickness are estimated fabrication errors according to [12]. Note that the frequency is given in $\Omega/2\pi$.

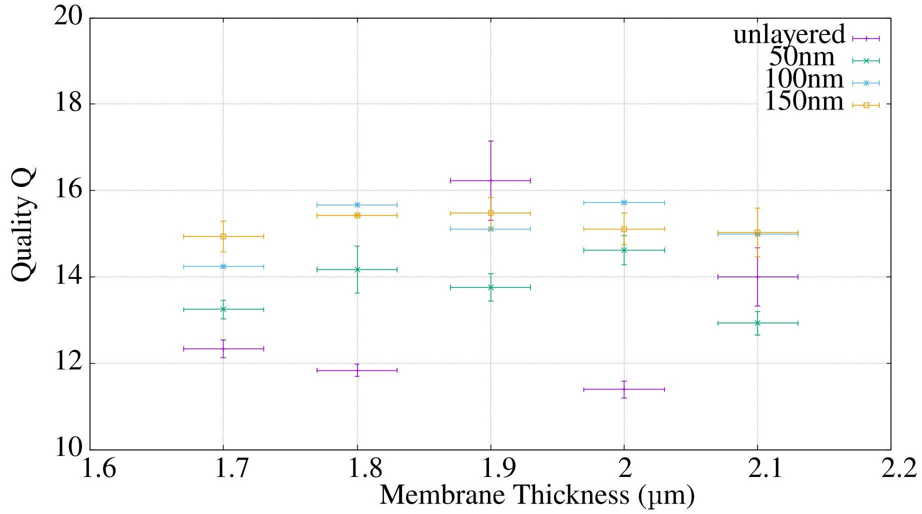

Figure 6.7: Measured data for the development of the average quality for different drum thicknesses and layer thicknesses. The errors on the membrane thickness are estimated fabrication errors according to [12].

It is worth to note, that the value for the unlayered membrane with 1.9 µm thickness has the highest measured quality (fig. 6.7), due to the lowest measured linewidth (see. fig. 6.8). This is due to a problem during the measurements of this drum thickness, in which only a single out of the 5 mentioned drum specimen had a small measurable response in the unlayered case. The result is therefore not averaged over many measurements and therefore the results for this membrane thickness (1.9 µm) are less meaningful.

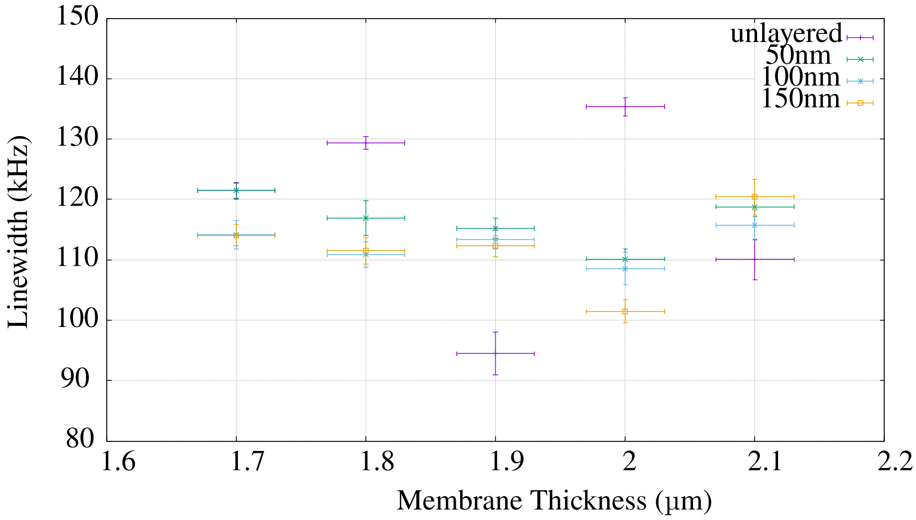

Figure 6.8: Development of the measured linewidth for different drum thicknesses and layer thicknesses. The errors on the membrane thickness are estimated fabrication errors according to [12]. Note that the linewidth is given in $\Gamma/2\pi$

Comparison with simulation Figure 6.9 shows a comparison between the measured and simulated data of a test drum, based on a 2.0 µm thick polymer membrane (see section 4.4.1). The comparison reveals a noticeable discrepancy between the measured and the simulated values for the drum. Though the simulated and measured data show a similar trend, they have a large offset in resonance frequency and quality. The reason for that is most likely due to the fact, that the fabricated drums have different membrane thicknesses than the ones programmed to the 3D printer and used for the simulations (c.f. fabrication limits of printer in section 5.2). While the actual diameter of the drums can be estimated with optical microscopy, the lateral size, especially the membrane thickness, could not be measured exactly in the lab. They can only be estimated (see section 5). The comparison with the simulations (see fig. 6.9) shows that quality improvements are in principle possible, but rather small and limited to $\sim$ 100 nm layers, since the effect quickly saturates with increasing layers.

Discussion The mechanical resonances at room temperature and atmospheric pressure were measured for polymer drums with varying thicknesses. The deposition of MgF_2 caused an overall resonance shift of the fundamental modes to higher frequencies. The measured values show a deviation from the simulations, which is probably due to the limits of the 3D printer. For the quality factor of the layered drums, differences of up to $\Delta Q \simeq +4.2$ could be observed, which is mainly due to the increase in resonance frequency rather than a decrease in linewidth. Since the qualities reached maximum values of about $Q \simeq 15.9$ the effect is also rather small compared to state of the art MIM applications like SiN membranes with qualities of up to 10^7 in vacuum [10]. The damping losses caused by the polymer are still dominant and limit the mechanical quality. This approach of layering the membranes has therefore only a marginal effect on the systems, since only the resonances get shifted slightly. Especially at room temperature ($T = 300$ K), where the thermal decoherences have a huge influence and high mechanical qualities are required (see eq. (4.6)), this layering approach has no significant impact. Since the measured and simulated data show a similar development (see fig. 6.9) of the qualities, only differing by an offset, one can estimate from the simulations that a repeat of

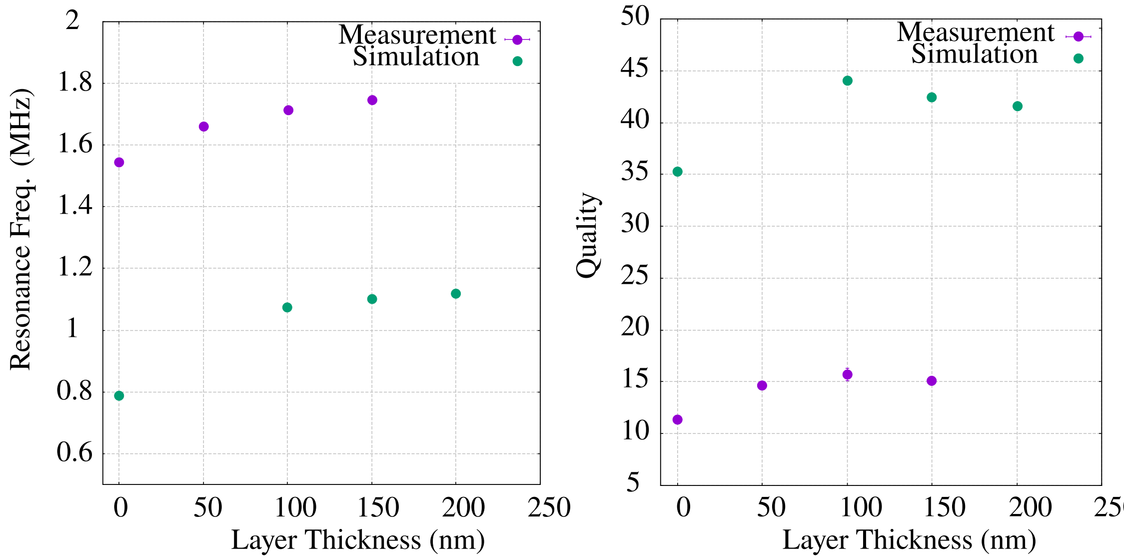

Figure 6.9: Comparison of measured and simulated data for a layered drum with polymer thickness of 2.0 µm. (Left) Resonance frequency. (Right) Quality

this measurement in vacuum would lead to similar results and only marginal quality improvements by the dielectric layer. It is therefore concluded that additional dielectric layers do not lead to big improvements on the mechanical properties of the polymer drums. The measured and simulated data show that small quality improvements with layer thickness up to 100 nm could be reached, but the effect quickly saturates and is too small to lead to a significant improvement of the systems.

6.3 Removal of Polymer beneath the MgF_2 Layer

As the findings of section 6.2 suggest, the mechanical qualities of the layered drums are still limited by the mechanical losses of the polymer membrane. A consequent next step is to reduce the thickness of the polymer membrane or even entirely remove it to reduce damping losses. As the simulations in section 4.4.1 suggest, with only the MgF_2 layer left, high mechanical quality systems ($Q > 160$) could be achieved from the approach of layering the polymer drums. For the removal, the idea is to use a plasma to etch away the polymer beneath the MgF_2 layer (see fig. 6.10).

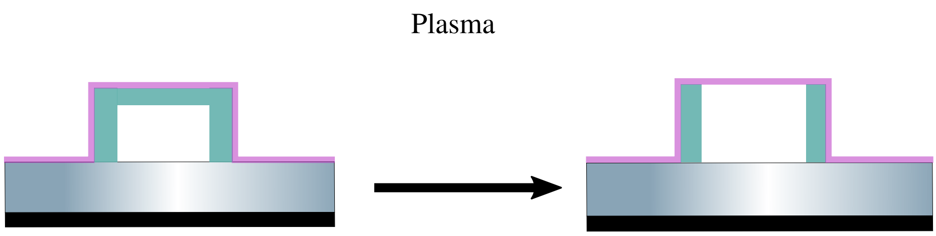

Figure 6.10: Polymer removal by plasma treatment.

For the drum geometries a few adjustments are made. Since the membranes need to get etched away evenly a fully circular design is used in contrast to the cut drums in the experiments in section

6.2. Since the structures get easily removed from the mirror surface during the plasma process, they need larger posts for a better adhesion to the surface, which on the other hand results in longer writing times. The used steplike structure of the posts (see fig. 6.11) combine both, a good adhesion to the surface, and a comparably short writing time for a large structure. Since this production procedure is prone to destroy the samples during each step, the drums were fabricated in multiple test arrays, with the same drum design for each sample. This increases the chances of having at least one good sample for a measurable response.

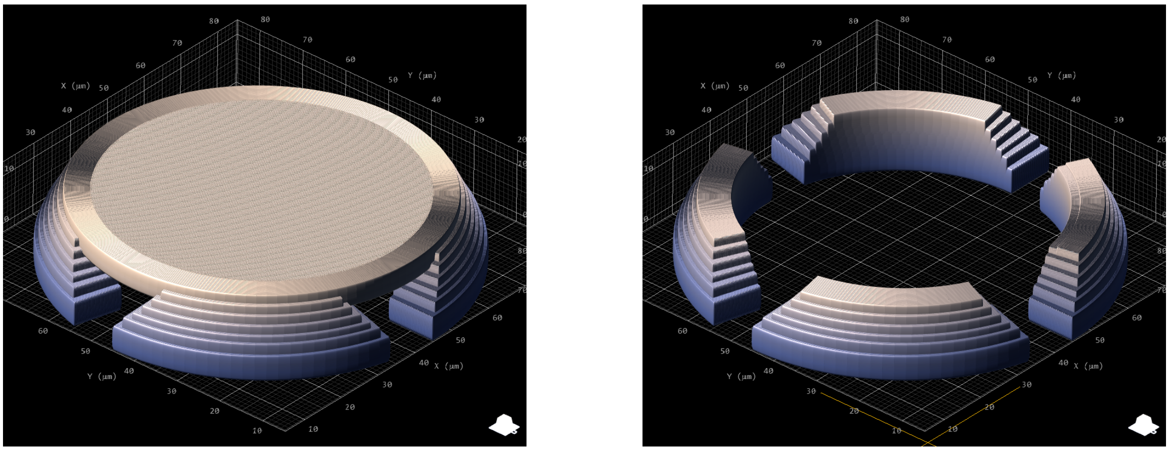

Figure 6.11: Depiction of the programmed structures in *DeScribe* [27]. (Left) The full drum structure used for the plasma burning tests and measurements. (Right) Steplike structure of the drum posts.

The main problem occuring, while trying to remove the polymer, were again cracks forming inside the MgF_2 layer (see fig. 6.12). As mentioned before, this was most probably due to the different thermal expansion coefficients of MgF_2 and IP-S [12, 33]. The cracks appear with most of the higher power settings in the plasma oven. To avoid cracks, the only option was to use very low powers, but with a very long process times. To avoid too long burning times, the removal of the polymer was done with two consecutive plasma runs. The first step of the production is the fabrication of a polymer drum

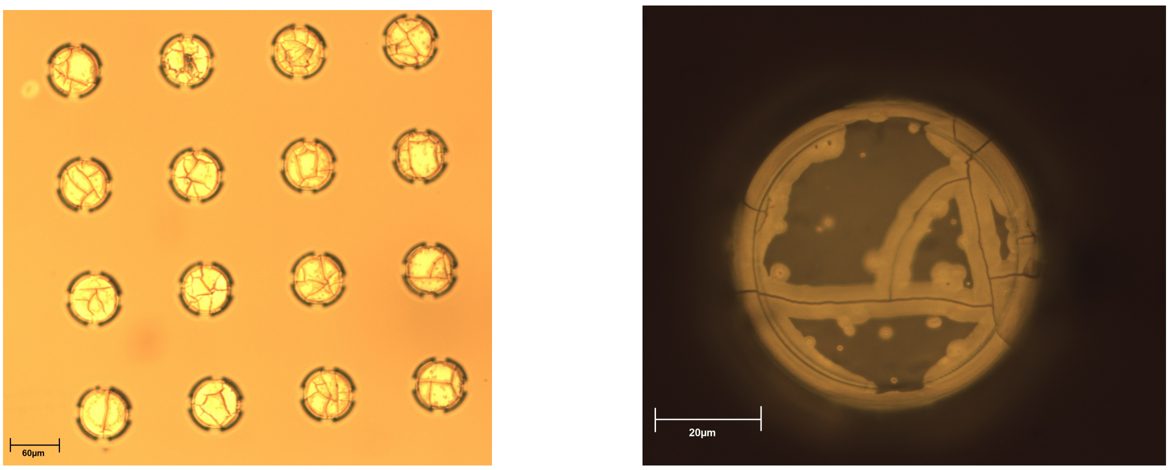

Figure 6.12: Optical microscope image of cracks inside MgF_2 layer after plasma process.

with smallest possible membrane thickness ~ 1 µm (according to *NanoScribe* [12]). This fabrication process turned out to be quite challenging. Since the membrane layers for this production are quite thin, they often tend to get ripped in the printing process, as mentioned before (see section 5.2). Various combinations of writing parameters have been trialled, until acceptable results could be achieve in *GalvoScanmode* with *ScanSpeed* of 15 000 µm/s and 96 % *LaserPower*. The drums were then treated with the first plasma run (25 min at 40 %) to etch away most of the polymer membrane, such that enough of the polymer membrane is left to be layered with MgF_2. For the evaporation a 100 nm layer of MgF_2 was used. This layer size turned out to have the most chances of surviving the plasma process and to stay on the remaining polymer posts. In the final step the polymer layer remaining beneath the MgF_2 gets etched down in a (second) 50 min plasma run with 5 % power (see fig. 6.13).

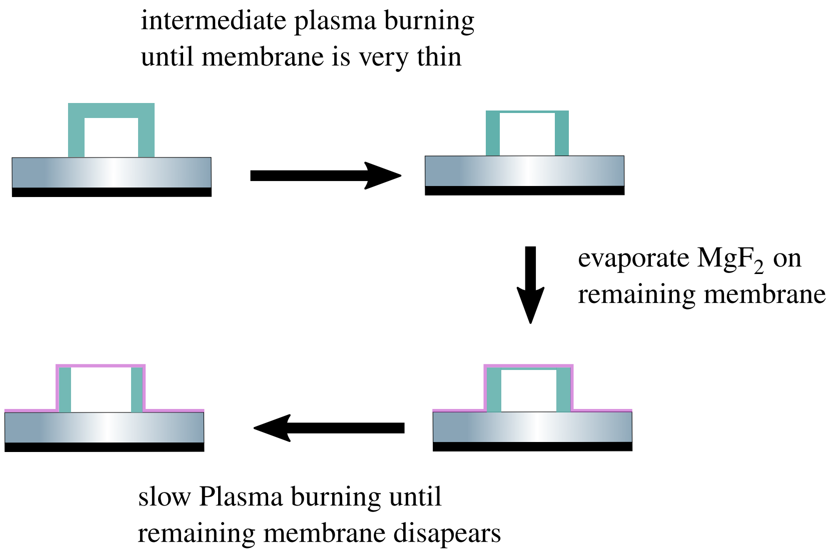

Figure 6.13: Process steps of polymer removal by plasma treatment.

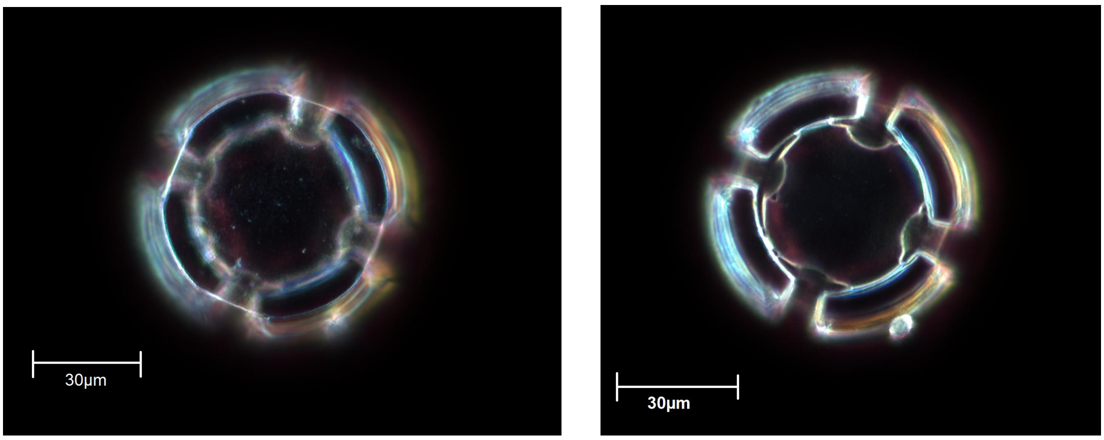

Figure 6.14: Dark field image of a sample with partially removed polymer layer. The left picture displays the upper drum layer, in which no visible cracks occur, like in fig. 6.12. The right picture shows the polymer layer in a different focus of the microscope. The polymer layer starts to disintegrate.

Results The proposed plasma removal process was applied to some test samples and the polymer membranes could be reduced without destroying the MgF_2 layer. However, with the applied process parameters, the MgF_2 layer could only be partially removed, which is demonstrated for a test drum in figure 6.14. It displays a test sample after the process in dark field image. One can see that no cracks occur in the Mg_2layer and in the focus of the polymer layer (see fig. 6.14 right) the polymer slightly disintegrates from the drum posts. After the partial removal the remaining samples were further measured in the free space setup. Since this measurement should only indicate, whether a drum with improved quality factor could be realised, the drum with the best measured values was chosen. The measured resonance of the sample with the best response is depicted in figure 6.15.

The measured sample exhibits a resonance frequency at 7.545 MHz and a quality factor of $Q = 20.04 \pm 0.09$. Comparing this to the simulations of a fully circular drum (see section 4.4.1), this result should correspond to a higher order mode. Compared to the qualities, achieved in section 6.2, the quality is rather large, but still in a low quality region. Due to supposedly less mechanical losses with reduced polymer membrane, it could be however interesting to measure this sample again in a cryogenic environment, which wasn't possible in my experiments due a limited time frame.

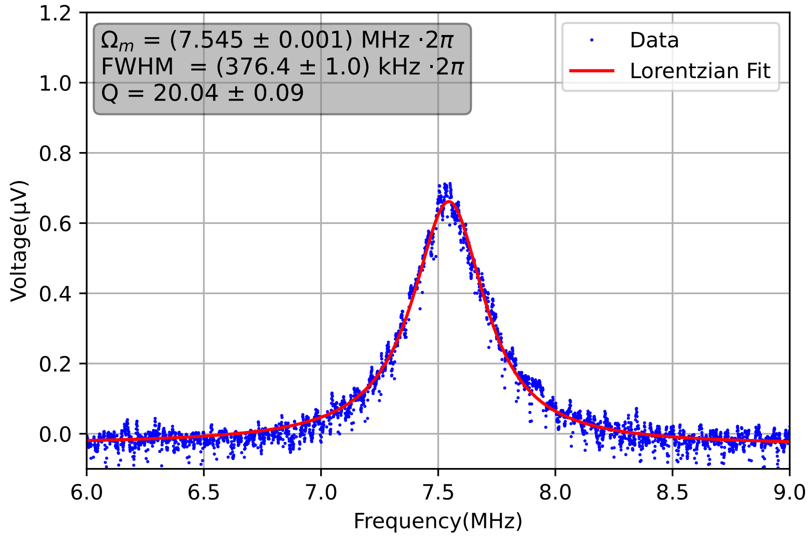

Figure 6.15: Resonance curve for a layered polymer drum (100 nm MgF_2) with partially removed polymer membrane.

6.4 Outlook: Couplingstrength of layered Membranes

In the last part of this thesis I wanted to further investigate the effect of a dielectric layer on the optomechanical couplingstrength of the polymer drum. Since the couplingstrength of a MIM system is governed by its boundary conditions, for a noticeable effect the difference in the refractive index between the polymer and dielectric layer should be rather large. A suitable material would be for example hafnium dioxide (HfO_2) with a refractive index of ($n(780\,\text{nm}) \simeq 1.9$ [42]). This would create higher reflection at the interface and could therefore potentially lead to higher frequency shifts (couplingstrengths).

For the evaporation of HfO_2 a system using an electron beam method is recommended rather than the thermal evaporation process, as used for MgF_2 [43]. Such a system was ordered for our lab, but unfortunately didn't arrive in time to be used for this test. Nevertheless I will briefly explain in the following how the expected optomechanical coupling of such a layered MIM system can be simulated.

6.4.1 Simulating the expected optomechanical Coupling

In this section the simulation of the coupling strength of such a layered MIM system, in contrast to the method of a single unlayered membrane, is discussed. Compared to the discussion of the fields

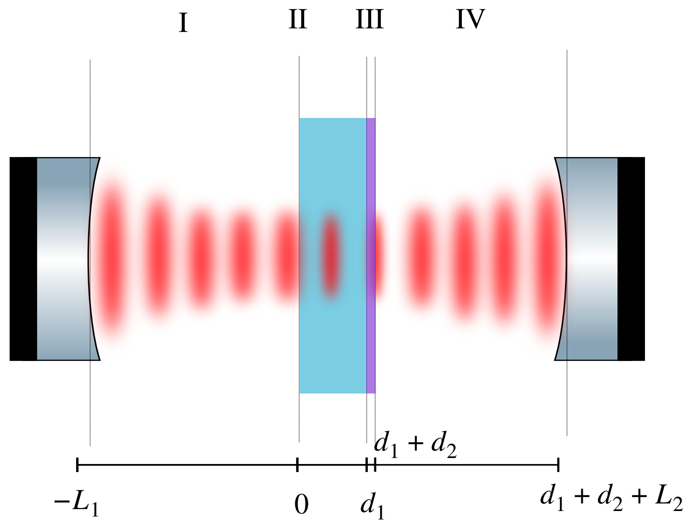

Figure 6.16: MIM system with layered membrane. The cavity system exhibits four different domains, in which a lightfield builds up.

inside an optomechanical MIM cavity with a single polymer membrane (see sec. 3.3), the situation for a layered membrane becomes more complicated (see fig. 6.16). The system now consists of 4 different domains, for which the individual electromagnetic fields and boundary conditions need to be considered. Trying to solve such a system analytically is quite challenging. However, the system can be elegantly solved by using a transfer matrix approach for this system, which considers the resulting frésnel reflections in each domain and interface (for further explanation of this formalism see for example [15]). With this method the cavity is treated as a partially transmittive optical system. For incident light, that gets coupled in at the first mirror and coupled out at the second one, the reflected and transmitted part after passing each domain and boundary is calculated. The entire system can then be described by one single transfer matrix **M** such that

$$\begin{pmatrix} U_2^{(+)} \\ U_2^{(-)} \end{pmatrix} = \mathbf{M} \begin{pmatrix} U_1^{(+)} \\ U_1^{(-)} \end{pmatrix}$$

$U_i^{(+)}$ describes the forward propagating and $U_i^{(-)}$ the backward propagating part of the light at each interface. The transfer matrix of the entire system is then simply derived by a multiplication of all individual transfer matrices for all domains and interfaces [15].

$$\mathbf{M} = \prod_i \mathbf{M}_i = \frac{1}{t_{21}} \begin{pmatrix} t_{12}t_{21} - r_{12}r_{21} & r_{21} \\ -r_{12} & 1 \end{pmatrix}$$

The reflectivity and transmittance of the systems are then defined as

$$R = |r_{12}|^2 \qquad , \qquad T = 1 - R$$

A cavity resonance is reached, if the transmitted part gets maximized and the reflected part minimized, which corresponds to T and R. With this the cavity resonance conditions, for constant cavity length L_{cav} and varying parameters ($L_1 \pm \Delta L, \omega_{cav} \pm \Delta\omega$) can be calculated. For given layered membrane thicknesses ($d_{polymer}$, d_{layer}) this simulation results in a sinosoidal resonance curve for $\omega_{cav}(L_1)$, in which L_1 describes the drum height respectively the membrane position (see white curve in figure 6.17). In figure 6.17 the resonance condition for different membrane positions (corresponding to $L_1 \pm \Delta L$) and laser frequencies is mapped exemplary.

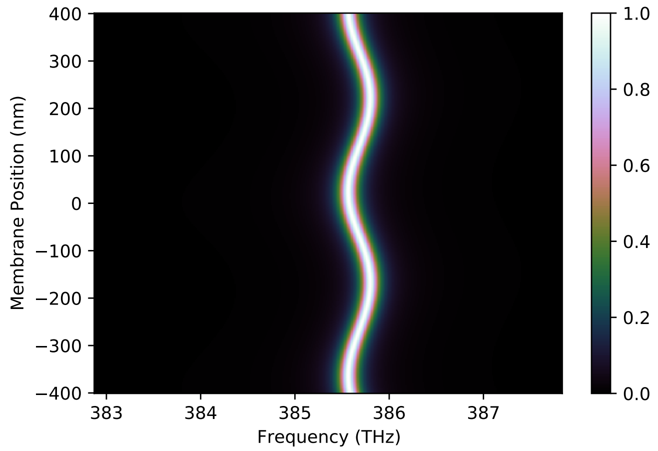

Figure 6.17: Example map of simulated cavity resonances for varying membrane position with sinusoidal behaviour of transmission maxima. It assumes a layered polymer membrane (L_1 = 10 µm, d_{pol} = 1 µm, n_{pol} = 1.51, d_{layer} = 30 nm, n_{layer} = 1.9) in a cavity (L_{cav} = 30 µm) and mirror reflectivity of R_i = 99%.

The couplingstrength of this system is defined as $g_0 = x_{ZPF} G^{(1)}$, which can be derived by simulating the linear pullparameter. Since the pullparameter is defined as the position dependent derivative of the cavity resonance,

$$G^{(1)} = \frac{\partial}{\partial x} \omega_{cav}$$

it can be derived from the sinosoidal $\omega_{cav}(L_1)$ by applying a sinus fit (with fit parameters a, b, c, d) to the sinusoidal resonance data (see fig. 6.17), from which then the positional derivative can be derived.

$$f(x) = a \cdot \sin(b \cdot x - c) + d$$
$$\frac{\partial}{\partial x} f(x) = a \cdot b \cos(b \cdot x - c)$$

From the derivative $\frac{\partial}{\partial x} f(x) \equiv \frac{\partial}{\partial x} \omega_{cav}(x)$ and the fit-parameters (a, b, c) the pullparameter can then be calculated. An example with the theoretically derived linear pullparameters, for such a HfO_2 layer on a polymer membrane with increasing layer thickness and drum heights, is mapped in figure 6.18. From figure 6.18 the pullparameter can now be estimated, which shows an oscillatory behaviour for

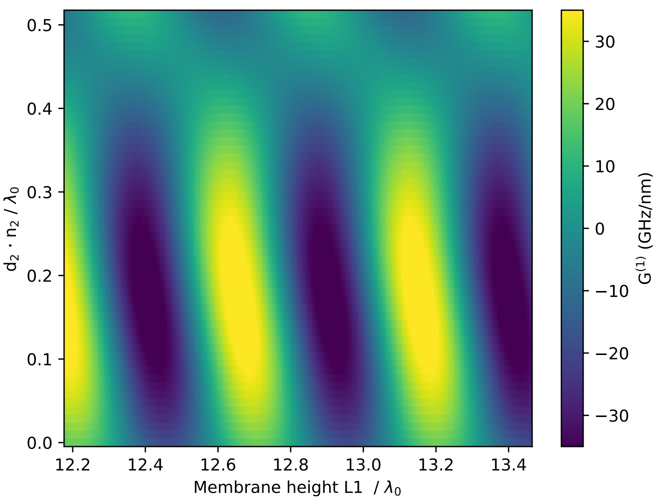

Figure 6.18: Mapped linear pullparameter for increasing HfO_2 layer thicknesses on a 2.0 µm thick polymer membrane and varying drum heights L_1, linearized to the material wavelength of the laser λ_0/n.

varying layer thickness (d_2) and height (L_1) behaviour with a period of one wavelength, similar to the single layer pullaparameter (see fig. 3.5).

According to the simulations, linear pullparameters of up to 35 GHz/nm could be theoretically achieved for the example polymer drum system layered with hafnium dioxide layers. If in agreement with experimental results, this approach of modeling an optomechanical systems by using a transfer matrix formalism can potentially offer a powerful tool to simulate arbitrary MIM systems with multiple membranes or layers.

CHAPTER 7

Conclusion and Outlook

Within the scope of this thesis the influence of dielectric layers on the mechanical properties of polymer drums, used as optomechanical MIM systems in fiber cavities at room temperature, was investigated. Magnesium fluoride (MgF_2) layers of several thicknesses were deposited onto direct laser written polymer drums. The fabrication of samples with sufficient quality was optimized.

Compared to the bare polymer membranes the measurements on drums with additional MgF_2 layers showed only small improvements of the overall mechanical qualities. With reaching quality improvements of up to $\Delta Q \simeq +4.2$, for 100 nm MgF_2 layers, this effect quickly saturates for thicker layers. The effect turned out to be mainly due to the accompanied increase in resonance frequency, caused by a higher overall young's modulus, rather than by a decrease in linewidth respectively a decrease of mechanical losses. With maximum reached qualities of $Q < 16$ the systems are still in a rather low quality regime compared to state of the art systems like SiN membranes with $Q \sim 10^6$ [9].

Since the polymer losses turned out to be still too dominant, it was further investigated, whether it was possible to remove the polymer membrane of the layered drums, leaving the dielectric layer with 100 nm MgF_2, and whether this would lead to further quality improvements. An air plasma process was used to remove the polymer beneath the dielectric layer and process parameters were optimized. However, with this method the polymer could only be removed to a certain degree until the structure fails. In the experiments the most prominent signals corresponded to higher order modes ($\Omega/2\pi \simeq 7.54$ MHz), with qualities of up to $Q \simeq 20$. This shows a slight improvement in quality compared to simply layered polymer drums, but is still in a low quality region.

Experiments at cryogenic temperatures have shown that the qualities of the polymer membranes could reach values of up to ~ 600 [11]. It could be therefore interesting to repeat the measurements with these layered samples and reduced polymer membrane at cryogenic temperatures. Within the time frame and also due to complications with the cryogenic setup these experiments were not possible.

In conclusion, the project didn't achieve the desired improvements of the mechanical properties of the polymer drums. The systems are still too strongly affected by the mechanical losses of the polymer. Though small improvements could be observed for 100 nm MgF_2 layers, their effect is yet too marginal for significant improvements of these systems.

A possible follow up project could be to measure the effect on the optomechanical couplingstrength of a layered polymer drum. For such an approach a high refractive index material like hafnium dioxide is recommended, which requires an electron beam evaporator. Since such a device was not available in time, this experiment couldn't be conducted within the frame of this thesis.

Bibliography

[1] V. B. Braginsky and *et al.*, *Quantum Nondemolition Measurements*, Science **209** (1980).

[2] V. Braginsky and A. Manukin, *Ponderomotive Effects of Electromagnetic Radiation*, Soviet Physics Journal of Experimental and Theoretical Physics (1967).

[3] P. Meystre, *A short walk through quantum optomechanics*, Annalen der Physik **525.3** (2012).

[4] H. Sun, Y. Liu and T. Li, *Application perspective of cavity optomechanical system*, Sec. Quantum Engineering **1** (2022).

[5] M. Aspelmeyer, T. J. Kippenberg and F. Marquardt, *Cavity Optomechanics*, Rev. Mod. Phys. **86** (2014).

[6] R. Burgwal and *et al.*, *Comparing nonlinear optomechanical coupling in membrane-in-the-middle and single-cavity systems*, New Journal of Physics **22** (2020).

[7] F. Brennecke and *et al.*, *Cavity Optomechanics with a Bose-Einstein Condensate*, Science **322** (2008).

[8] M. Eichenfeld and *et al.*, *Optomechanical Crystals*, Nature **462** (2009).

[9] B. M. Zwickl and *et al.*, *High quality mechanical and optical properties of commercial silicon nitride membranes*, Appl. Phys. Lett. **92** (2008).

[10] J. D. Thompson and *et al.*, *Strong dispersive coupling of a high-finesse cavity to a micromechanical membrane*, Nature **452** (2008).

[11] L. Tenbrake and *et al.*, *Direct laser-written optomechanical membranes in fiber Fabry-Perot cavities*, `https://doi.org/10.1007/s00340-022-07752-8` (2023).

[12] NanosGuide, *Customer support webside NanoScribe*, `https://support.nanoscribe.com`, [Online; accessed 24-March-2023].

[13] L. Tenbrake, *Fiber Cavity Optomechanics with Polymer Membranes*, Universität Bonn, 2021.

[14] H. Pfeiffer and *et al.*, *Achievements and perspectives of optical Fiber Fabry-Perot Cavities*, Appl. Phys. B **128** (2022).

[15] B. E. A. Saleh and M. C. Teich, *Fundamentals of Photonics (Ed. 3)*, Wiley, USA 2019.

[16] D. Meschede, *Optik, Licht und Laser*, Vieweg+Teubner Verlag, Bonn 2008.

[17] M. Kubista, *A New Fiber Mirror Production Setup*, 2017.

[18] D. Hunger and *et al.*, *A fiber Fabry–Perot cavity with high finesse*, New J. Phys. **12** (2010).

[19] J. D. Jackson, *Klassische Elektrodynamik*, de Gruyter, Berlin 1981.

[20] M. Schmid, D. Ludescher and H. Giessen, *Optical properties of photoresists for femtosecond 3D printing: refractive index, extinction, luminescence-dose dependence, aging, heat treatment and comparison between 1-photon and 2-photon exposure*, Opt. Mater. Express **9** (2019).

[21] M. A. Meyers and K. K. Chawla, *Mechanical Behavior of Materials*, Cambridge University Press, Cambridge 2009.

[22] E. Ventsel and T. Krauthammer, *Thin Plates and Shells: Theory, Analysis, and Applications*, Marcel Dekker, Pennsylvania 2001.

[23] X. Shi et al., *A unified method for free vibration analysis of circular, annular and sector plates with arbitrary boundary conditions*, Journal of Vibration and Control **22** (2014).

[24] M. Gologanu et al., *Damping Effects in MEMS Resonators*, International Semiconductor Conference (CAS) **1** (2012).

[25] D. M. Karabacak and *et al.*, *High-Frequency Nanofluidics: An Experimental Study Using Nanomechanical Resonators*, Phys. Rev. Lett. **98** (2007).

[26] COMSOL, *Structural Mechanics Module User's Manual*, 2018.

[27] Nanoscribe-GmbH, *Nanoscribe Photonics Professional GT User Manual*, 2015.

[28] O. Stein and *et al.*, *Fabrication of Low-Density Shock-Propagation Targets Using Two-Photon Polymerization*, Fusion Science and Technology **73** (2018).

[29] E. D. Lemma and *et al.*, *Mechanical Properties Tunability of Three-Dimensional Polymeric Structures in Two-Photon Lithography*, IEEE Transactions on Nanotechnology **16** (2017).

[30] Robert C. L. N. Kramer and *et al.*, *Multiscale 3D-printing of microfluidic AFM cantilevers*, Lab Chip **20** (2019).

[31] F. Brückerhoff-Plückelmann, *Dielectric Waveguide Fabrication by Direct Laser Writing*, Universität Bonn, 2019.

[32] A. Reuß, *Herstellung eines Faser-zu-Rechteckwellenleiter Kopplers mittels Laserlithographie*, Universität Bonn, 2020.

[33] Crystran Ltd - World Wide Optics Source, *MgF_2 data sheet*, `https://www.crystran.co.uk/optical-materials/magnesium-fluoride-mgf2`, [Online; accessed 02-Mai-2023].

[34] P. Lopez-Reyes and *et al.*, *Optimization of the deposition parameters of MgF2/LaF3 narrowband reflective FUV multilayers*, Optical Materials Express **11** (2021).

[35] P. Makkar and *et al.*, *Development and properties of duplex MgF2/PCL coatings on biodegradable magnesium alloy for biomedical applications*, PLoS One **13** (2018).

[36] A. Munitz and *et al.*, *Dynamic Mechanical Analysis of pure Mg and Mg AZ31 Alloy*, Magnesium Technology **2004** (2004).

[37] Kurt J.Lesker Company, *Thermische Verdampfung von Magnesiumfluorid (MgF2)*, `https://de.lesker.com/newweb/deposition_materials/depositionmaterials_evaporationmaterials_1.cfm?pgid=mg2`, [Online; accessed 11-Mai-2023].

[38] Umberto M. B. Marconi and *et al.*,
Fluctuation-Dissipation: Response Theory in Statistical Physics, Physics Reports **461** (2008).

[39] M. L. Gorodetksy, V. Yakhot and K. L. Ekinci,
Determination of the vacuum optomechanical coupling rate using frequency noise calibration, Optics Express **18** (2010).

[40] Toptica Photonics AG, *General Error-Signal Generation Schemes: Side-of-fringe locking*, `https://www.toptica.com/application-notes/phase-and-frequency-locking-of-diode-lasers/error-signal-generation/general-error-signal-generation-schemes`, [Online; accessed 02-Mai-2023].

[41] Newport Corporation, *Introduction to Laser Frequency Stabilization*, `https://www.newport.com/n/introduction-to-laser-frequency-stabilization`, [Online; accessed 02-Mai-2023].

[42] M. Al-Kuhaili,
Optical properties of hafnium oxide thin films and their application in energy-efficient windows, Optical materials **27** (2004).

[43] Kurt J.Lesker Company, *Hafnium Oxide HfO_2 Evaporation Process Notes*, `https://de.lesker.com/newweb/deposition_materials/deposition-materials-notes.cfm?pgid=hf2`, [Online; accessed 11-Mai-2023].

List of Figures

List of Tables

Acknowledgement

At this small space at the end of my thesis I want to give some notes of thanks. First of all I want to thank Professor Stefan Linden for letting me write my masters thesis in his Nanophotonics group and all his support during the time of my thesis. Secondly I want to thank Professor Sebastian Hofferberth for agreeing to be the second corrector of my thesis. I also want to thank all the wonderful people from the Nanophotonics group and the Fiberlab for all their help and support during the entire time. Especially I want to thank Lukas Tenbrake, Alexander Fassbender and Dr. Hannes Pfeiffer for their guidance in the Laboratory and for all of their helpful ideas and thoughts on the experiments.